Article
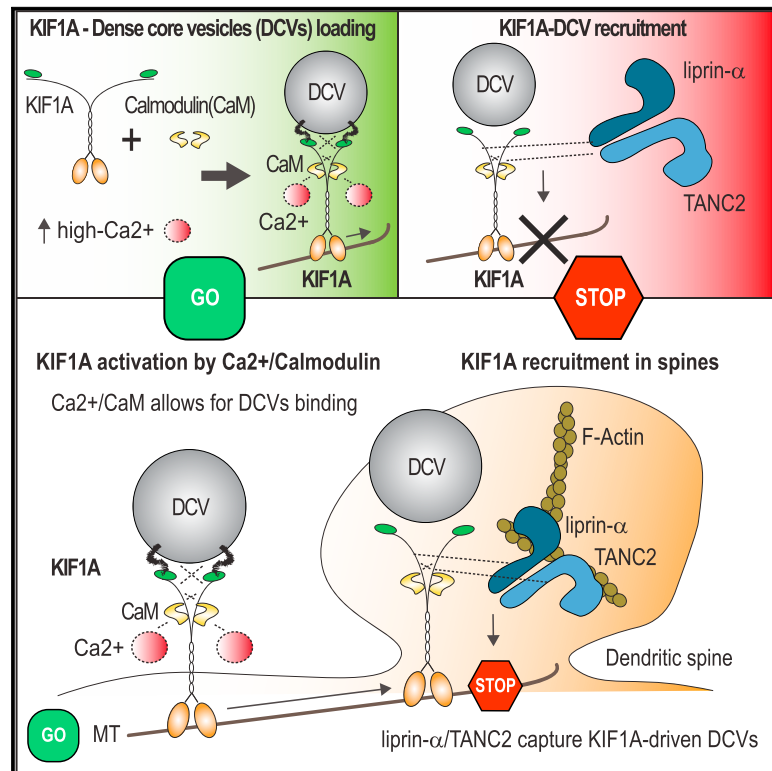
Regulation of KIF1A-Driven Dense Core Vesicle Transport: Ca²⁺/CaM Controls DCV Binding and Liprin-α/TANC2 Recruits DCVs to Postsynaptic Sites

Graphical Abstract

Authors

Riccardo Stucchi, Gabriela Plucińska, Jessica J.A. Hummel, ...,
Richard A. Scheltema,
A.F. Maarten Altelaar,
Casper C. Hoogenraad

Correspondence

c.hoogenraad@uu.nl

In Brief

Stucchi et al. show that KIF1A-dependent transport is regulated by CaM, liprin-α, and TANC2. KIF1A binding to DCVs is controlled by a Ca²⁺/CaM molecular mechanism, and KIF1A-driven DCVs are recruited in dendritic spines by the PSD scaffolds liprin-α and TANC2.

Highlights

- KIF1A directly interacts with CaM and with the scaffolds liprin-α and TANC2

- KIF1A is regulated by a Ca²⁺/CaM-dependent mechanism, which allows for DCV loading

- Liprin-α and TANC2 are static PSD proteins that are not part of the KIF1A-DCV complex

- KIF1A-driven DCVs are recruited to dendritic spines by liprin-α and TANC2

Data and Software Availability

PXD010080

CellPress

Regulation of KIF1A-Driven Dense Core Vesicle Transport: Ca²⁺/CaM Controls DCV Binding and Liprin-α/TANC2 Recruits DCVs to Postsynaptic Sites

Riccardo Stucchi,[1,2,3] Gabriela Plucińska,[1] Jessica J.A. Hummel,[1] Eitan E. Zahavi,[1] Irune Guerra San Juan,[1] Oleg Klykov,[2,3] Richard A. Scheltema,[2,3] A.F. Maarten Altelaar,[2,3] and Casper C. Hoogenraad[1,4,*]

[1]Cell Biology, Department of Biology, Faculty of Science, Utrecht University, Padualaan 8, 3584 Utrecht, the Netherlands
[2]Biomolecular Mass Spectrometry and Proteomics, Bijvoet Center for Biomolecular Research and Utrecht Institute for Pharmaceutical Sciences, Utrecht University, Padualaan 8, 3584 Utrecht, the Netherlands
[3]Netherlands Proteomics Centre, Padualaan 8, 3584 Utrecht, the Netherlands
[4]Lead Contact
*Correspondence: c.hoogenraad@uu.nl
https://doi.org/10.1016/j.celrep.2018.06.071

SUMMARY

Tight regulation of neuronal transport allows for cargo binding and release at specific cellular locations. The mechanisms by which motor proteins are loaded on vesicles and how cargoes are captured at appropriate sites remain unclear. To better understand how KIF1A-driven dense core vesicle (DCV) transport is regulated, we identified the KIF1A interactome and focused on three binding partners, the calcium binding protein calmodulin (CaM) and two synaptic scaffolding proteins: liprin-α and TANC2. We showed that calcium, acting via CaM, enhances KIF1A binding to DCVs and increases vesicle motility. In contrast, liprin-α and TANC2 are not part of the KIF1A-cargo complex but capture DCVs at dendritic spines. Furthermore, we found that specific TANC2 mutations—reported in patients with different neuropsychiatric disorders—abolish the interaction with KIF1A. We propose a model in which Ca²⁺/CaM regulates cargo binding and liprin-α and TANC2 recruit KIF1A-transported vesicles.

INTRODUCTION

Kinesins and dyneins are motor proteins responsible for cargo transport and delivery along microtubule tracks. Microtubule-based cargo transport is particularly important in cells with complex geometry, such as neurons (Hirokawa et al., 2010). The neuronal transport machinery delivers proteins, lipids, mRNA, and organelles to the distal sites, as well as controlling cargo degradation and recycling of building blocks. Various cargoes that are transported along microtubules move bidirectionally, exhibiting periods of rapid movements, pauses, and directional switches. The identification of mutations in genes encoding tubulin isoforms, motor proteins, or other components of the trafficking machinery in human patients strongly supports the view that defective cargo transport can directly trigger neurode-generation (Millecamps and Julien, 2013). It is therefore impor-

tant to understand how cargo trafficking is initiated and how cargoes are captured at their final destinations. In addition, transport deficits might arise through various indirect mechanisms. For example, the stalling of vesicles could trigger the formation of aggregates within axons that may result in neuronal dysfunction.

Several molecular mechanisms related to microtubules, motors, and cargo interactions were shown to regulate cargo pick-up and delivery (Maeder et al., 2014; Schlager and Hoogenraad, 2009). On one hand, microtubule orientation, length, and spacing in axons and dendrites can control cargo sorting and transport efficiency (Kapitein et al., 2010; Yogev et al., 2016). Additional motor-microtubule mechanisms include tubulin post-translational modifications (PTMs), microtubule-associated proteins (MAPs), and tubulin isotypes (Gumy et al., 2017; Sirajuddin et al., 2014). On the other hand, transport is regulated on the site of motor-cargo interaction through motor interaction with phospholipids, receptors or integral membrane proteins, scaffolding proteins, and small Rab guanosine triphosphatase (GTPases) and their effector proteins (Maeder et al., 2014; Schlager and Hoogenraad, 2009). Moreover, local subcellular specializations and compartmentalization of specific structures can control local cargo trafficking. For instance, the axon initial segment (AIS) functions as a cargo filter that selectively prevents passage of dendritic vesicles while allowing the entry of axonal cargoes (Leterrier and Dargent, 2014). Furthermore, evidence suggests that during transient microtubule polymerization into dendritic spines, kinesin motors transport cargoes along microtubules (MTs) into spines (Esteves da Silva et al., 2015; McVicker et al., 2016). Despite growing evidence of transport regulation, little is known about how vesicles are loaded on motors and captured at the dendritic spines.

KIF1A, named UNC-104 in *Caenorhabditis elegans (C. elegans)* and *Drosophila,* was identified as the primary motor protein first for synaptic vesicles (SVs) (Niwa et al., 2008; Okada et al., 1995) and later for dense core vesicles (DCVs) (Barkus et al., 2008; Lo et al., 2011; Zahn et al., 2004). DCVs, also called secretory vesicles or post-Golgi vesicles, are transported from the Golgi apparatus to the plasma membrane in both axons and dendrites, unlike SVs (de Wit et al., 2006; Lochner et al., 2008). DCVs contain secretory proteins such as brain-derived
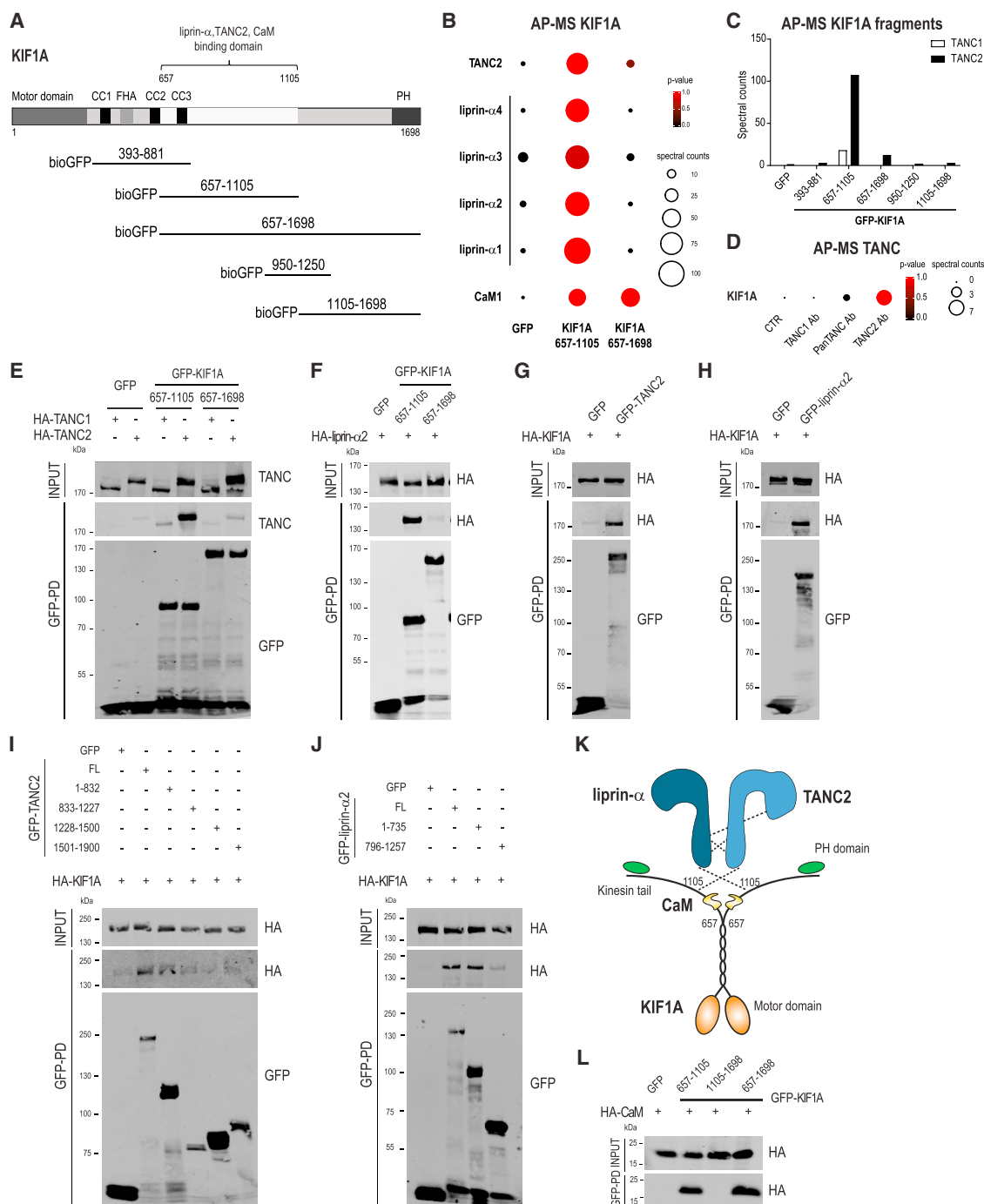
Figure 1. KIF1A Binds to TANC2, Liprin-α, and CaM

(A) bioGFP-KIF1A(383-881, 657-1105, 657-1698, 950-1250, 1105-1698) used to perform AP-MS experiments.

(B) KIF1A interactors identified by MS. p values and spectral counts are graphically represented by colors and spheres, respectively. See also Figures S1A and S1B and Tables S1 and S2.

(C) TANC1 and TANC2 spectral counts detected by MS.

(D) TANC (TANC1 Ab, PanTANC Ab, and TANC2 Ab) immunoprecipitation-MS experiments. p values and spectral counts of KIF1A are graphically represented by colors and spheres, respectively.

(E) Western blots (WBs) of HA-TANC proteins and liprin-α1 in AP experiments of bioGFP-KIF1A(657-1105, 657-1698) from co-transfected HEK293 cells.

(F) WB of HA-liprin-α2 in AP of bioGFP-KIF1A(657-1105, 657-1698).

(G and H) WB of HA-KIF1A in AP of bioGFP-TANC2 (G) or bioGFP-liprin-α2 (H).

(legend continued on next page)

neurotrophic factor (BDNF) and neuropeptide Y (NPY) and do not coincide with membrane protein transferrin receptor (TfR) (Lipka et al., 2016). The integral membrane protein synaptotagmin 4 (Syt4) is also present on DCVs (Dean et al., 2009). The scaffolding protein liprin-α interacts with the tail region of KIF1A (Shin et al., 2003), and liprin-α mutants in *Drosophila* impair cargo trafficking, suggesting that liprin-α is part of the KIF1A-cargo complex (Miller et al., 2005). However, in *C. elegans,* liprin-α is mainly localized to synaptic sites, and its distribution is not affected in KIF1A mutants (Sieburth et al., 2005). An additional model suggests that liprin-α can play an active role in clustering KIF1A-transported SVs (Wagner et al., 2009; Wu et al., 2013). Thus, whether liprin-α is a cargo adaptor linking KIF1A to vesicles or captures KIF1A-driven cargo to synaptic sites remains an open question.

To better understand how KIF1A-driven vesicle trafficking is controlled in neurons, we performed an interactome analysis of KIF1A. Based on those results, we focused on three KIF1A binding partners, the calcium binding protein calmodulin (CaM) and two synaptic scaffolding proteins: liprin-α and TANC2 (tetratricopeptide repeat, ankyrin repeat, and coiled coil containing 2). TANC2 was originally identified as a postsynaptic density (PSD)-95-interacting protein, regulating dendritic spine and synapse function (Han et al., 2010). TANC2 gene mutations are identified in patients with neurological disorders ranging from autism to schizophrenia (de Ligt et al., 2012; Fromer et al., 2014; Iossifov et al., 2012). To gain insights into the role of these three proteins in KIF1A-mediated transport, we used a combination of live-cell imaging and biochemical-proteomic methodology. This approach allowed us to demonstrate that calcium, acting via CaM, enhances KIF1A binding to DCVs and increases vesicle motility. In addition, we show that liprin-α and TANC2 are mainly localized in dendritic spines and recruit KIF1A-driven DCVs to synaptic sites. Altogether, our findings reveal a mechanism for pick-up and delivery of DCVs in dendrites.

RESULTS

Kinesin-3 Family Member KIF1A Interacts with Liprin-α and TANC2

KIF1A contains a classical N-terminal motor domain, followed by three coiled coils, a stalk domain in the middle part, and a pleckstrin homology (PH) domain in the tail region, which in *C. elegans* is crucial for recognition of phosphatidylinositol 4,5-bisphosphate (PIP_2) in cargo vesicle membranes (Figure 1A) (Klopfenstein et al., 2002). To identify KIF1A interactome, we set up a systematic affinity purification-mass spectrometry (AP-MS) screening using different KIF1A tail fragments (Figure 1A). BioGFP-KIF1A fragments were expressed in HEK293 cells, purified with streptavidin beads, and incubated with brain lysates. Co-isolated proteins were then analyzed by mass spectrometry (MS). Among the list of putative interacting proteins detected with this approach, we classified candidate KIF1A binding part-

ners with a probability > 0.98, using SAINT (Significance Analysis of INTeractome) to score our AP-MS data (Figure S1A; Tables S1 and S2) (Choi et al., 2011). Most identified binding partners are associated with the stalk domain of KIF1A (amino acid 657-1105), and most of them belong to the postsynaptic density (PSD) (7.82 = −log10[corrected − p value] Gene Ontology [GO], cellular component) (Figures S1A and S1B). This stalk region is highly similar to MAGUK binding sites (MBSs) found in other kinesin-3 motors, such as KIF13B (Zhu et al., 2016). MBS regions mediate binding with the guanylate kinase (GK) domain, and in the case of KIF13B, MBS is required for the formation of a complex with the GK of the synaptic protein DLG1 (Hanada et al., 2000; Yamada et al., 2007). Although MBS regions are highly conserved, small amino acid sequence variations could drastically change their binding specificities for different scaffolding proteins. In line with this, our results indicate that the MBS domain of KIF1A interacts with a different group of postsynaptic scaffolds compared to KIF13B, confirming high selectivity of these domains (Figure S1A; Tables S1 and S2). As part of the interactome, we detected well-known interactors of KIF1A, such as liprin-α family proteins (Shin et al., 2003), as well as interactors such as TANC2. We observed a highly significant enrichment of TANC2 total spectral counts (Figure 1B) but not of counts for its homolog TANC1 (Figure 1C). Similarly, we found KIF1A associated only with TANC2 in our AP-MS experiment in which we immunoprecipitated TANC1 or TANC2 from rat brain extracts (Figure 1D). To validate our proteomic results, we performed affinity purification-Western blot (AP-WB) experiments in cells co-expressing bioGFP-KIF1A fragments (657-1105 and 657-1698), along with a hemagglutinin (HA)-tagged version of TANC1 and TANC2. As expected, both TANC2 and liprin-α bound the KIF1A middle fragment (657-1105), but not TANC1 (Figures 1E and 1F). Surprisingly, neither TANC2 nor liprin-α was able to bind a longer KIF1A fragment including the PH domain (Figures 1E and 1F), as shown by MS data (Figure 1B; Tables S1 and S2), indicating an auto-inhibitory role of the C-terminal portion of KIF1A. As final evidence, reverse AP-WB experiments confirmed that TANC2 and liprin-α are binding partners of KIF1A (Figures 1G and 1H), and *in vitro* competition assays showed that TANC2 and liprin-α2 partially compete for the same binding site on KIF1A (Figures S1C and S1D). In addition, we pinpointed their N-terminal domains as the regions mainly involved in the binding (Figures 1I and 1J; Figure S1F). We also found a potential association between TANC2 and liprin-α (Figures S1G and S1H); however, it is quite likely that the two proteins only indirectly interact by binding KIF1A within a macromolecular complex. Overall, these results identify the PSD proteins liprin-α and TANC2 as interactors of KIF1A (Figure 1K).

Kinesin-3 Family Member KIF1A Interacts with CaM
Among other identified candidate KIF1A interactors, we decided to further characterize the calcium regulator CaM. As suggested by the number of CaM spectra detected by MS (Figure 1B) and

(I) WB of HA-KIF1A in AP of full-length GFP-TANC2 and GFP-TANC2 fragments (1-832, 833-1227, 1228-1500, and 1501-1900).
(J) WB of HA-KIF1A in AP of full-length GFP-liprin-α2 and GFP-liprin-α2 fragments (1-735 and 796-1257).
(K) Schematic representation of KIF1A in association with the PSD scaffolding proteins TANC2 and liprin-α2 and with the calcium sensor CaM.
(L) WB of HA-CaM in AP of bioGFP-KIF1A fragments (657-1105, 1105-1698, and 657-1698).
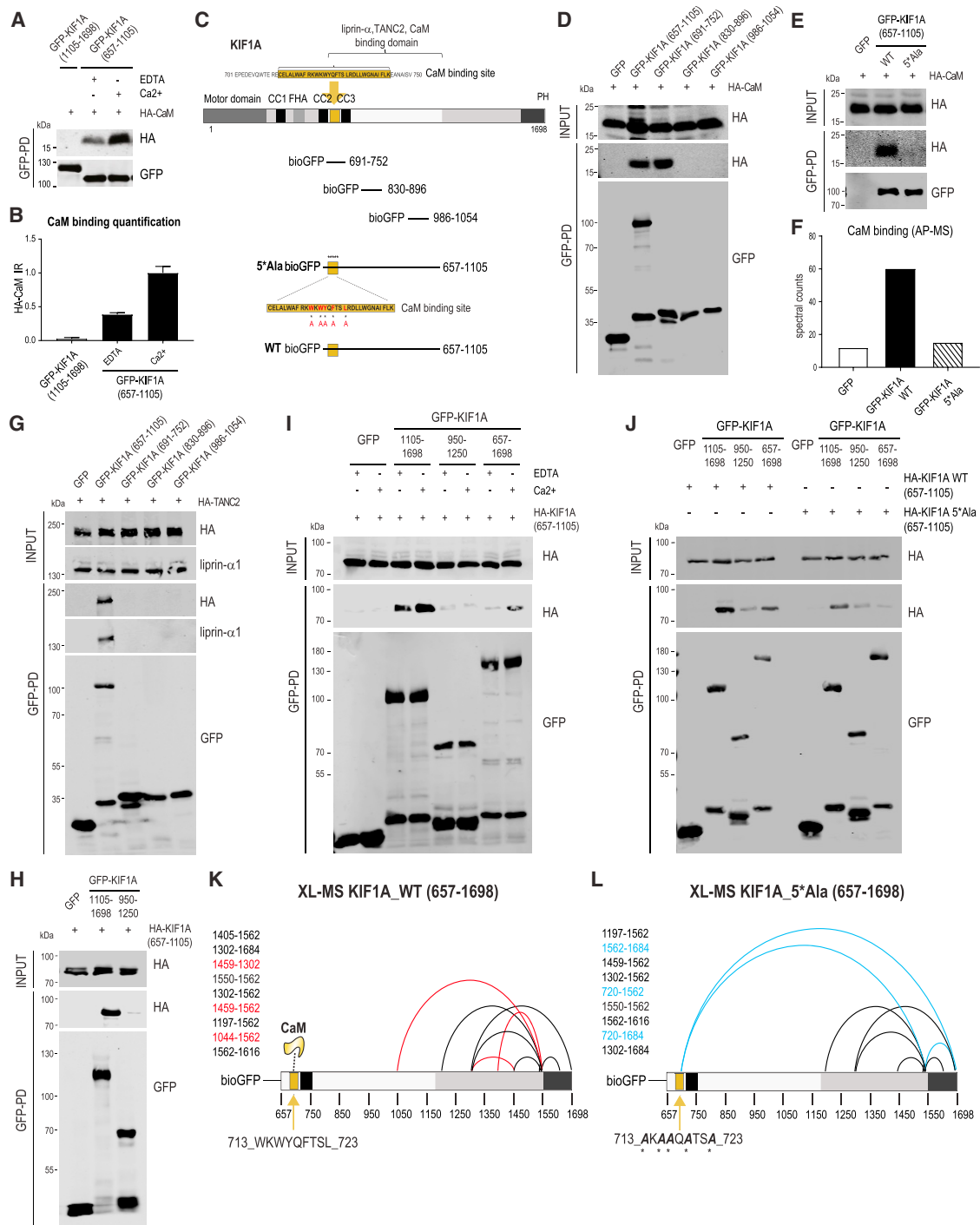
Figure 2. Ca²⁺ Promotes CaM-KIF1A Binding and Ca²⁺/CaM Modulates KIF1A Tail Conformation

(A) bioGFP-KIF1A(657-1105) was expressed in HEK293 cells, purified using streptavidin pull-downs, and incubated with protein extracts of cells expressing HA-CaM in the presence of 2 mM EDTA or 2 mM Ca²⁺. bioGFP-KIF1A(1105-1698) was used as negative control. Western blot detection was performed using HA and GFP antibodies.

(B) Quantification of CaM relative intensities shown in (A), calculated as the ratio of HA-CaM signals normalized on the affinity-purified bioGFP-KIF1A signals. n = 3 experiments per condition. The bars show mean ± SEM.

(C) bioGFP-KIF1A fragments (691-752, 800-896, and 986-1054) and mutant bioGFP-KIF1A(657-1105_5*Ala) (W714A, W716A, Y717A, F719A, and L722A).

(D) WB of HA-CaM in AP experiments of bioGFP-KIF1A truncations (657-1105, 691-752, 800-896, and 986-1054) from co-transfected HEK293 cells.

(E) WB of HA-CaM in AP of bioGFP-KIF1A(657-1105_WT) or bioGFP-KIF1A(657-1105_5*Ala).

(legend continued on next page)

confirmed by subsequent AP-WB (Figure 1L), CaM is one of the few proteins capable of binding both the KIF1A middle tail region (657-1105) and the full tail (657-1698). Combined with CaM being calcium regulated, it represents an ideal modulator of KIF1A-based cargo trafficking (Figure 1K). Typically, calcium binding to the EF hands of CaM induces a conformational switch, which exposes the hydrophobic pockets present in the two lobes of CaM, allowing binding to target proteins (Zhang et al., 1995). To assess the ability of CaM to bind to KIF1A in response to calcium, we performed *in vitro* affinity purification (AP) assays using bioGFP-KIF1A fragments and HA-CaM in the presence of excessive calcium (2 mM) or EDTA (2 mM) (Wang and Schwarz, 2009). Western blot (WB) analysis revealed that the amount of CaM bound to KIF1A increased by ∼50% in calcium-supplemented samples (Figures 2A and 2B), indicating a stronger association between motor protein and CaM upon calcium addition.

The structure of Ca^{2+}-bound CaM is flexible and dynamic, allowing it to recognize and modulate the activity of its substrates. As a consequence, the consensus sequence for CaM binding motifs is not well defined. Most Ca^{2+}/CaM binding substrates can be broadly characterized by a short stretch of amino acids containing a high density of positively charged and hydrophobic residues (Yamniuk and Vogel, 2004). In search of potential CaM binding sites, we used two separate databases: the Calmodulin Target Database (http://calcium.uhnres.utoronto.ca) (Yap et al., 2000) and the Calmodulation Database and Meta-Analysis website (http://cam.umassmed.edu) (Mruk et al., 2014). This analysis revealed the existence of a conserved binding motif for CaM spanning residues 710–740 of KIF1A (Figure 2C). Therefore, we generated different KIF1A fragments of ∼60 amino acids each (Figure 2C) and found that KIF1A(691-752) interacted with CaM (Figure 2D). Consequently, we made a CaM binding-deficient bioGFP-KIF1A(657-1105) fragment by substituting five hydrophobic amino acids with alanine residues, as reported previously (Figure 2C) (Li and Sacks, 2003). The absence of HA-CaM signal and of CaM spectra in the bioGFP-KIF1A_5*Ala pull-downs indicates that the hydrophobic residues are required for CaM recognition (Figures 2E and 2F). Altogether, these results indicate that CaM interacts with a short KIF1A fragment (691-752), in contrast to TANC2 and liprin-α, which require the entire region (657-1105) to associate with KIF1A (Figure 2G) and do not compete with CaM for KIF1A binding (Figures S1C–S1E).

CaM Binding to KIF1A Changes Intramolecular Interactions

Next, we wanted to address the question of the loss of KIF1A binding partners in the full-length fragment. As described earlier,

TANC2 and liprin-α are able to bind to KIF1A(657-1105), but not to the longer fragment KIF1A(657-1698) (Figures 1B, 1E, and 1F; Figure S1A). One possible explanation is the presence of an inhibitory mechanism caused by the intramolecular interactions. To assess this, we performed AP-WB experiments using different bioGFP-KIF1A truncations, in combination with HA-KIF1A(657-1105). We only detected binding between HA-KIF1A(657-1105) and bioGFP-KIF1A(1105-1698), confirming an intramolecular interaction between the C terminus and the middle part of the tail (Figure 2H). This interaction is regulated by Ca^{2+}/CaM binding (Figures 2I and 2J). To further characterize these intramolecular interactions, we applied crosslinking-mass spectrometry (XL-MS) to KIF1A(657-1698_WT) and mutant KIF1A(657-1698_5*Ala). We detected nine intramolecular cross-linked peptides, of which 6 peptides were shared between the two proteins (in black) (Figures 2K and 2L). Three of those cross-links were specific for either KIF1A-wild-type (WT) (highlighted in red) or KIF1A_5*Ala (in blue). In the KIF1A_5*Ala mutant, crucial intramolecular interactions were disturbed compared to the WT protein. In particular, crosslink 1044-1562 was not present in the absence of CaM and aberrant intramolecular crosslinks 720-1562 and 720-1684 were detected, confirming that the backfolding of the tail is governed by CaM binding.

Ca^{2+}/CaM Regulates the Binding of KIF1A with DCVs

Altogether, our results highlight the importance of Ca^{2+}/CaM in regulating KIF1A molecular dynamics. In the following steps, we decided to repeat our initial KIF1A AP-MS experiments in rat brain extracts, this time supplemented with either calcium or EDTA (Figures 3A–3C). The number of spectra detected for co-precipitated liprin-α and TANC2 markedly decreased in samples treated with calcium when compared to the EDTA condition (Figures 3A and 3C; Figure S2A), suggesting that calcium negatively affects the binding affinity of KIF1A for these scaffolds. Consistent with the *in vitro* AP data (Figures 2A and 2B), we detected more CaM spectra in the presence of calcium compared to the EDTA condition (Figures 3A–3C). Only in the presence of calcium KIF1A(657-1698) associated with specific DCV-related proteins such as Syt4 and synaptotagmin 11 (Syt11) (Figures 3B and 3C; Figure S2B). We obtained the same results for other proteins involved in PIP_2 and phosphoinositide metabolism (Figure 3C; Figures S2C–S2E). Based on these results, we can conclude that calcium increases the binding between KIF1A and DCVs. These proteomic findings were confirmed by *in vitro* AP-WB experiments (Figures 3D–3I). Using a CaM binding-deficient KIF1A mutant (657-1698_5*Ala), revealed a reduction in the amounts of co-precipitated Syt4 (Figure 3J) or Syt11

(F) CaM spectral counts detected by MS in AP of bioGFP-KIF1A(657-1105_WT) or bioGFP-KIF1A(657-1105_5*Ala).

(G) WB of HA-TANC2 and liprin-α1 in AP of bioGFP-KIF1A(657-1105, 691-752, 800-896, 986-1054).

(H) WB of HA-KIF1A(657-1105) in AP of bioGFP-KIF1A(1105-1698, 950-1250).

(I) bioGFP-KIF1A(1105-1698, 950-1250, 657-1698) were incubated with protein extracts of cells expressing HA-KIF1A(657-1105) in the presence of 2 mM EDTA or 2 mM Ca^{2+}. WB detection was performed using HA and GFP antibodies. Ca^{2+} increases binding affinity between KIF1A fragments.

(J) bioGFP-KIF1A(1105-1698, 950-1250, 657-1698) were incubated with protein extracts of cells expressing HA-KIF1A(657-1105_WT) or HA-KIF1A(657-1105_5*Ala). WB detection was performed using HA and GFP antibodies. Mutant KIF1A(657-1105_5*Ala) shows reduced binding to KIF1A C-terminal fragments compared to WT.

(K and L) Crosslinking-mass spectrometry (XL-MS)-based analysis of purified bioGFP-KIF1A(657-1698_WT) (K) or bioGFP-KIF1A(657-1698_5*Ala) (L). Schematic maps of intra-protein crosslinks are identified. Crosslinks detected in both WT and 5*Ala are represented as black lines, WT-specific crosslinks are represented as red lines, and 5*Ala-specific crosslinks are represented as blue lines.
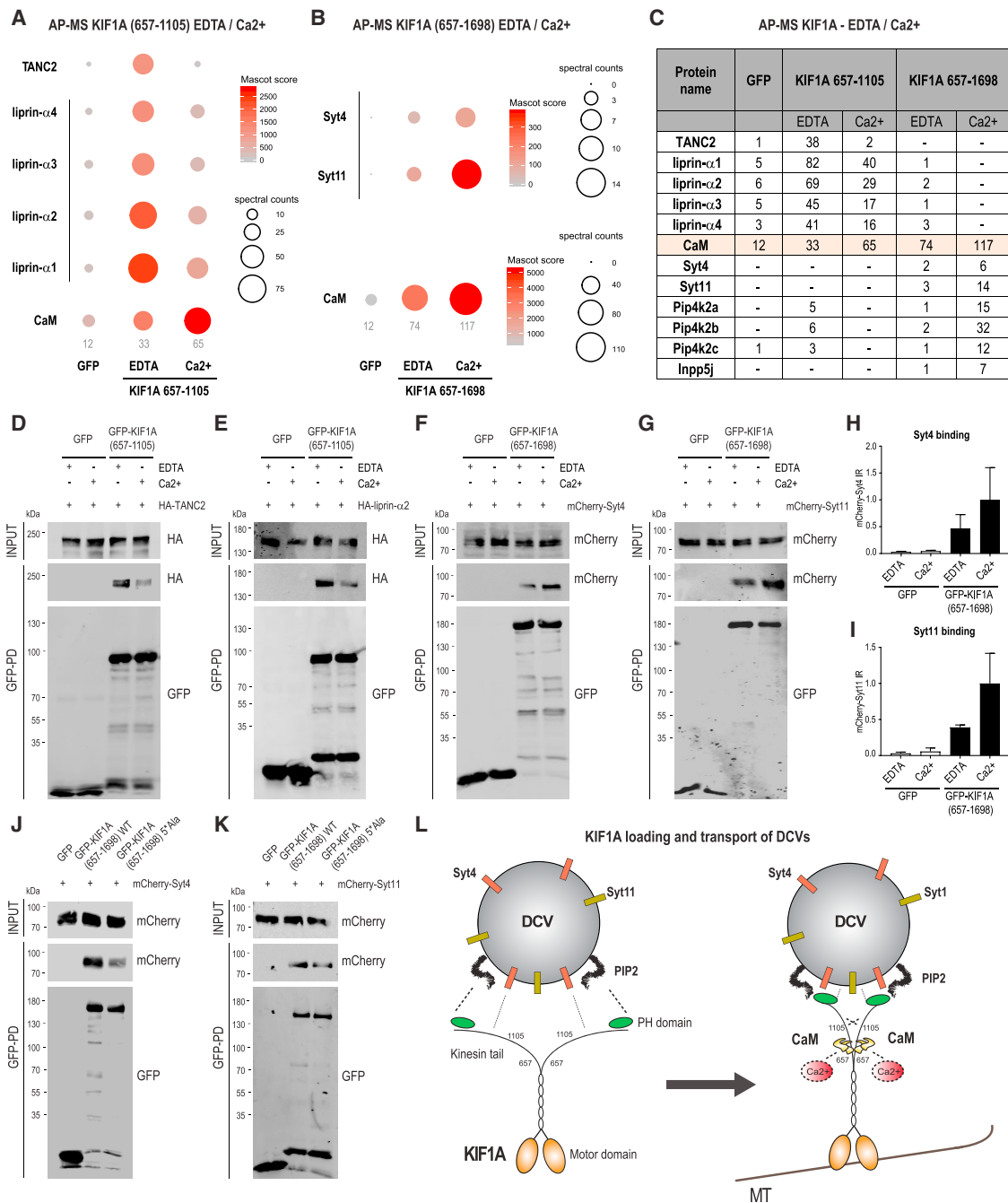
Figure 3. KIF1A Binds DCVs in a Ca^{2+}/CaM-Dependent Manner

(A) bioGFP-KIF1A(657-1105) was purified using streptavidin pull-downs and incubated with rat brain extracts in the presence of 2 mM EDTA or 2 mM Ca^{2+}. KIF1A(657-1105) interactors were identified by MS. Mascot scores and spectral counts of selected proteins (TANC2, liprin-α, and CaM) are graphically represented by colors and spheres, respectively. See also (C) and Figure S2A.

(B) bioGFP-KIF1A(657-1698) was incubated with rat brain extracts in the presence of 2 mM EDTA or 2 mM Ca^{2+}. KIF1A(657-1698) interactors were identified by MS. Mascot scores and spectral counts of selected proteins (Syt4, Syt11, and CaM) are graphically represented by colors and spheres, respectively. See also (C) and Figures S2B–S2E.

(C) Table represents the number of spectral counts detected in AP-MS experiments of bioGFP-KIF1A(657-1105) and bioGFP-KIF1A(657-1698) in the presence of 2 mM EDTA or 2 mM Ca^{2+} for selected co-purified proteins: TANC2, liprin-α, calmodulin (CaM), synaptotagmin (Syt), phosphatidylinositol 5-phosphate 4-kinase (Pip4k2), and inositol polyphosphate 5-phosphatase (Inpp5).

(D and E) bioGFP-KIF1A(657-1105) was incubated with protein extracts of cells expressing HA-TANC2 (D) or HA-liprin-α2 (E) in the presence of 2 mM EDTA or 2 mM Ca^{2+}. WB detection was performed using HA and GFP antibodies.

(legend continued on next page)

(Figure 3K), confirming a role for CaM in promoting the interaction between KIF1A tail and DCV proteins (Figure 3L). Our proteomic data did not allow us to derive any conclusion about SV-related proteins, because the number of spectra identified was not sufficient to show enrichment. Based on these considerations and taking into account that KIF1A(657-1105) was found associated with proteins enriched in the PSD (Figures S1A and S1B), we decided to further investigate the role of KIF1A in DCV trafficking in dendrites. First, we assess the role of CaM in the KIF1A-DCV interaction in hippocampal neurons. To this end, we co-expressed GFP-KIF1A_WT or GFP-KIF1A_5*Ala with DCV proteins: NPY-RFP (Figures 4A and 4B) or mCherry-Syt4 (Figures 4C and 4D). KIF1A-WT co-localized with NPY and Syt4 on vesicles, whereas mutant KIF1A, which is unable to bind CaM, showed a diffuse cytoplasmic localization that did not coincide with DCVs (Figures 4A–4E). Because CaM-KIF1A binding affinity is already stimulated at low micromolar concentrations of calcium (Figures 4F and 4G) (comparable to physiological Ca^{2+} concentrations in vivo), we next wondered whether increasing calcium in neurons could activate KIF1A-mediated DCV transport. To test this, we increased intracellular concentration of calcium by treating neurons with bicuculline, which acutely enhances neuronal activity by inhibiting γ-aminobutyric acid (GABA) receptor activity. Bicuculline induced clustering of KIF1A and increased motility of KIF1A-NPY complexes within minutes (Figures 4H–4M). In addition, we examined the effect of calcium deprivation (BAPTA-AM treatment) on DCV motility, and BAPTA-AM-treated neurons showed lower motility of KIF1A, NPY, and Syt4 vesicles (Figures 4N–4P). These data strongly support a role for calcium in the regulation of KIF1A-DCV loading and motility in neurons. Altogether, these results indicate that binding of Ca^{2+}/CaM to the KIF1A tail regulates DCV pick-up and trafficking (Figure 3L).

KIF1A-Mediated DCV Trafficking Is Independent of TANC2 and Liprin-α

Next, we were interested whether KIF1A, TANC2, and/or liprin-α can also control DCV motility. We first systematically quantified the co-localization of KIF1A with DCV markers (NPY, Syt4, and Syt11) in hippocampal neurons (Figure 5A; Figures S3A and S3B). KIF1A showed ~50% co-localization with NPY-, Syt4-, and Syt11-positive vesicles (Figures 5B and 5C). Next, we tested whether NPY and synaptotagmins label the same DCV population. Only 10% of the NPY-positive vesicles coincided with Syt4 or Syt11 (Figures 5D–5F; Figures S3C and S3D). In contrast, Syt4 and Syt11 showed ~70% co-localization (Figures 5G–5I; Figures S3E and S3F), indicating that NPY and synaptotagmins label different subpopulations of DCVs.

Second, using live-cell imaging, we assessed whether NPY and DCVs are transported by KIF1A. Kymographs of those re-cordings showed robust co-movement of GFP-KIF1A and NPY-RFP, as well as mCherry-Syt4-labeled vesicles (Figures 5J and 5K). Next, we tested the effect of KIF1A knockdown on NPY or Syt4 vesicle motility. DCV motility was severely affected in neurons depleted of KIF1A, with ~50% reduction of mobile NPY-GFP- or Syt4-Cherry-positive vesicles compared to pSuper control (Figures 5L–5O). We confirmed the specificity of this result with a rescue experiment in which expression of full-length KIF1A (but not of KIF1A lacking the C-terminal PH domain) restored NPY motility (Figure 5M). These data are in line with a previously described role for KIF1A in transporting DCVs (Arthur et al., 2010; Lipka et al., 2016; Lo et al., 2011; McVicker et al., 2016).

Finally, we assessed whether the depletion of TANC2 and/or liprin-α also affects DCV motility. We used previously described short hairpin RNAs (shRNAs) targeting liprin-α (Spangler et al., 2013) and generated TANC2-specific shRNAs, whose efficacy was tested by quantifying the intensity of the staining of endogenous TANC2 in neurons (Figures S3G–S3I). TANC2 or liprin-α knockdowns did not influence DCV motility, as shown by live-cell imaging of NPY or Syt4 (Figures 5N and 5O). In addition, other transport parameters, such as pausing frequency and duration, were not affected by this treatment (Figures S3J–S3L). These data suggest that TANC2 and liprin-α are not part of the KIF1A-DCV transport complex and do not work as classical cargo-adaptor proteins.

TANC2 and Liprin-α Are Scaffolding Proteins in Dendritic Spines

To better understand the roles of TANC2 and liprin-α in KIF1A-dependent cargo trafficking, we investigated their distribution in neurons. Both proteins localized in dendrites (Figure 6A), were enriched in dendritic protrusions, and co-localized with the postsynaptic markers PSD-95 and Homer (Figures 6B–6D). When co-expressed, TANC2 and liprin-α co-clustered in dendritic spines (Figure 6E). Analysis of the truncated isoforms revealed that the C-terminal part of TANC2 (1501-1900), which includes the PDZ binding domain, is responsible for the synaptic localization (Figure S4A). In contrast, for liprin-α, the N-terminal part (1-735) is required for the synaptic localization (Figure S4B). We followed those observations and characterized the interactomes of TANC2 and liprin-α (Tables S3 and S4). Based on this analysis, we identified postsynaptic density proteins (GO classification, cellular component), such as PSD-95(DLG4), SAP-97(DLG1), CASK, Scribble, Centaurin gamma2 and 3 (AGAP1 and AGAP3), and various subunits of the NMDA receptor (Grin1 and Grin2B), as the main interactors of TANC2 (Figure S4C; Table S3). These results are in line with previous findings that describe TANC2 as a synaptic scaffold, interacting and co-localizing with the synaptic anchoring proteins PSD-95

(F and G) bioGFP-KIF1A(657-1698) was incubated with protein extracts of cells expressing mCherry-Syt4 (F) or mCherry-Syt11 (G) in the presence of 2 mM EDTA or 2 mM Ca^{2+}. WB detection was performed using mCherry and GFP antibodies.

(H and I) Quantifications of Syt4 (H) and Syt11 (I) relative intensities shown in (F) and (G), calculated as the ratio of co-purified mCherry signals normalized on the bioGFP-KIF1A. n = 3 experiments per condition. The bars show mean ± SEM.

(J and K) bioGFP-KIF1A(657-1698_WT) or bioGFP-KIF1A(657-1698_5*Ala) was incubated with protein extracts of cells expressing mCherry-Syt4 (J) or mCherry-Syt11 (K). WB detection was performed using mCherry and GFP antibodies.

(L) Schematic model illustrating the Ca^{2+}-CaM mechanism acting on the KIF1A tail, leading to DCV loading and mobilization.
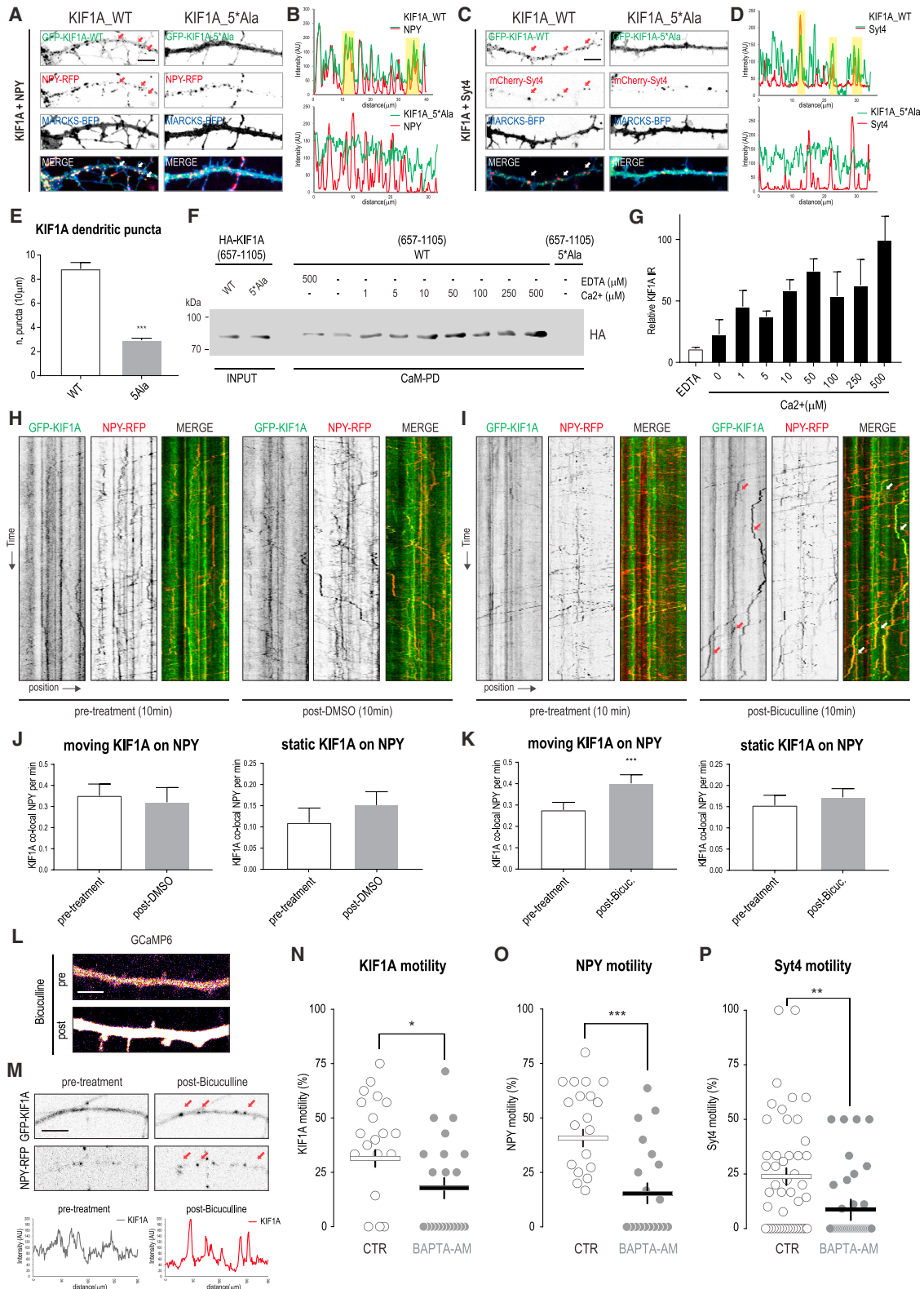
Figure 4. KIF1A-Driven DCVs Transport Is Regulated by Ca^{2+}/CaM

(A) Representative dendrites of rat hippocampal neurons (11–14 DIV) co-transfected with GFP-KIF1A_WT or GFP-KIF1A_5*Ala (green) with NPY-RFP (red). Arrows point to co-localizing puncta. Scale bar, 5 μm.

(legend continued on next page)

and Homer (Han et al., 2010) and with other PDZ domain proteins (Gasparini et al., 2017). Among the interacting partners of liprin-α2, we picked up both postsynaptic (Grip1, Grip2, Lin7, Trio, and CASK) (Wyszynski et al., 2002) and pre-synaptic proteins (Rims1/2, ERC1/2, and Munc13-1/2) involved in the maturation, docking and secretion of SVs and known to form macromolecular protein complexes with liprin-α in the axonal active zone (Figure S4D; Table S4) (Olsen et al., 2005; Spangler et al., 2013). Altogether, we can conclude that TANC2 and liprin-α are enriched in dendritic spines and interact with various synaptic proteins.

TANC2, KIF1A, and Liprin-α Depletion Affects Spine Density and Morphology

Spine morphology is largely controlled by actin dynamics. Identifying TANC2 and liprin-α as enriched in dendritic spines led us to speculate that their distribution and accumulation may also be regulated by actin. Therefore, we transfected neurons with GFP-TANC2 or GFP-liprin-α2 and treated them with either latrunculin B to depolymerize the actin cytoskeleton or jasplakinolide to stabilize actin (Figures S4E and S4F). Latrunculin B treatment reduced the number of TANC2 and liprin-α2 clusters in spines by ~30%, whereas jasplakinolide treatment resulted in an opposite phenotype, with ~30% increase of clusters in spines (Figures S4G and S4H). These data suggest that the localization and clustering of TANC2 and liprin-α2 are affected by the actin cytoskeleton in dendritic spines. This hypothesis is strengthened by the ability of several TANC2- and liprin-α-interacting proteins to directly or indirectly associate with the actin cytoskeleton (Figure S4I). To get further insights into the roles of TANC2, KIF1A, and liprin-α in dendritic spine morphology, we performed knockdown experiments. TANC2 depletion caused a significant reduction in the total number of protrusions, particularly of mushroom spines (Figure 6F), and the effect was rescued by re-introducing full-length TANC2 (Figure 6F). KIF1A and liprin-α depletion showed a similar phenotype, severely affecting the total number of dendritic protrusions (Figure 6H). These data are consistent with previous findings (Han et al., 2010; McVicker et al., 2016) and show that TANC2, KIF1A, and liprin-α depletion affects spine number and morphology.

TANC2 and Liprin-α2 Act as Immobile Postsynaptic Posts Able to Recruit KIF1A in a Subset of Dendritic Spines

Based on the preceding results, we further examined the functional relationship between KIF1A and TANC2 or liprin-α in dendritic spines. Co-expression of HA-KIF1A with GFP-TANC2 or GFP-liprin-α2 showed that ~10% KIF1A-FL co-clustered with TANC2 and liprin-α2 in dendritic spines (Figure 7A). In contrast, KIF1A(1-1105), lacking the PH domain but containing the TANC2 and liprin-α binding region, showed a rather diffuse cytoplasmic pattern (Figure 7B). Nevertheless, we noticed accumulation of KIF1A(1-1105) in dendritic spines that co-localized with TANC2 and liprin-α2 (Figure 7B), suggesting that KIF1A can co-localize with TANC2 and liprin-α2 in spines even without cargo binding. This effect was exacerbated when these proteins were expressed in COS7 cells (Figures S5A–S5F). Because KIF1A is a motor protein, we next examined the spatial and temporal dynamics of KIF1A, DCVs (by imaging NPY and Syt4), TANC2, and liprin-α. As we described earlier, KIF1A-, NPY-, and Syt4-positive vesicles showed high motility along the dendritic shaft. This was not the case for TANC2 and liprin-α, which were relatively static in dendritic spines (Figures 7C–7E). This finding supports our claim that TANC2 and liprin-α are not part of the KIF1A-DCV transport complex. Closer analysis of the vesicle dynamics revealed that DCVs frequently paused and stopped near TANC2- or liprin-α-positive clusters (Figures 7C–7E) and the number of DCV pauses at TANC2/liprin-α2 clusters was higher in mature neurons (17 days in vitro [DIV]) in which TANC2 and liprin-α2 were more accumulated in spines (Figures S5G–S5K). We also found DCV accumulation in dendritic spines, and in ~10% of the spines, DCVs co-localized with TANC2 and liprin-α2 (Figures 7F and 7G). To gain additional functional insight, we analyzed the distribution of DCVs in TANC2- or liprin-α-depleted neurons. TANC2 and liprin-α knockdown, but not Cortactin knockdown, caused a reduction of KIF1A, NPY, and Syt4 clusters in spines by ~40% compared to control (Figures 7H–7J). Based on these results, we propose that TANC2 and liprin-α recruit KIF1A-driven DCVs to dendritic spines (Figure 7K).

(B) Line scans of fluorescence intensity of GFP-KIF1A and NPY-RFP channels shown in (A).

(C) Dendrites of neurons co-transfected with GFP-KIF1A_WT or GFP-KIF1A_5*Ala (green) with mCherry-Syt4 (red). Arrows point to co-localizing puncta. Scale bar, 5 μm.

(D) Line scans of fluorescence intensity of GFP-KIF1A and mCherry-Syt4 channels shown in (C).

(E) Quantifications of GFP-KIF1A_WT and GFP-KIF1A_5*Ala puncta in dendrites. The bars show mean ± SEM (n = 20–28 dendrites; ***p < 0.001, t test).

(F) Ca^{2+} dependence of the in vitro binding of CaM to KIF1A. AP of CaM (anti-CaM beads) from lysates of cells transfected with HA-KIF1A(657-1105_WT) or HA-KIF1A(657-1105_5*Ala). WB detection was performed using anti-HA antibody.

(G) Quantification of KIF1A binding to CaM shown in (F). The percentage of maximal binding to CaM was defined as the intensity of the co-precipitated band of KIF1A and set at 100% in 2 mM Ca^{2+}. n = 3 experiments per condition. The bars show mean ± SEM.

(H and I) Representative kymographs showing trajectories of GFP-KIF1A and NPY-RFP vesicles in selected neurites of co-transfected neurons pre- and posttreatment with DMSO (H) or with 40 μm of bicuculline (I).

(J and K) Quantifications of trajectories of GFP-KIF1A co-localizing with NPY-RFP (see H and I) pre- and posttreatment with DMSO (J) or with bicuculline (K). The bars show mean ± SEM (n = 12 dendrites in J and n = 34 dendrites in K; ***p < 0.001, paired t test).

(L) Intracellular calcium levels in a representative dendrite treated with bicuculline and visualized with the calcium indicator GCaMP6. Scale bar, 5 μm.

(M) GFP-KIF1A clustering in a representative dendrite treated with bicuculline. Scale bar, 5 μm.

(N–P) Quantifications of the percentage of mobile GFP-KIF1A (N), NPY-GFP vesicles (O), or mCherry-Syt4 vesicles (P) in neurons (11–14 DIV) treated with DMSO (CTR) or 10 μm of BAPTA-AM. Bars show the mean (n = 21–29 dendrites in N, n = 20–28 dendrites in O, and n = 41–50 dendrites in P; *p < 0.05, **p < 0.001, ***p < 0.001, t test).
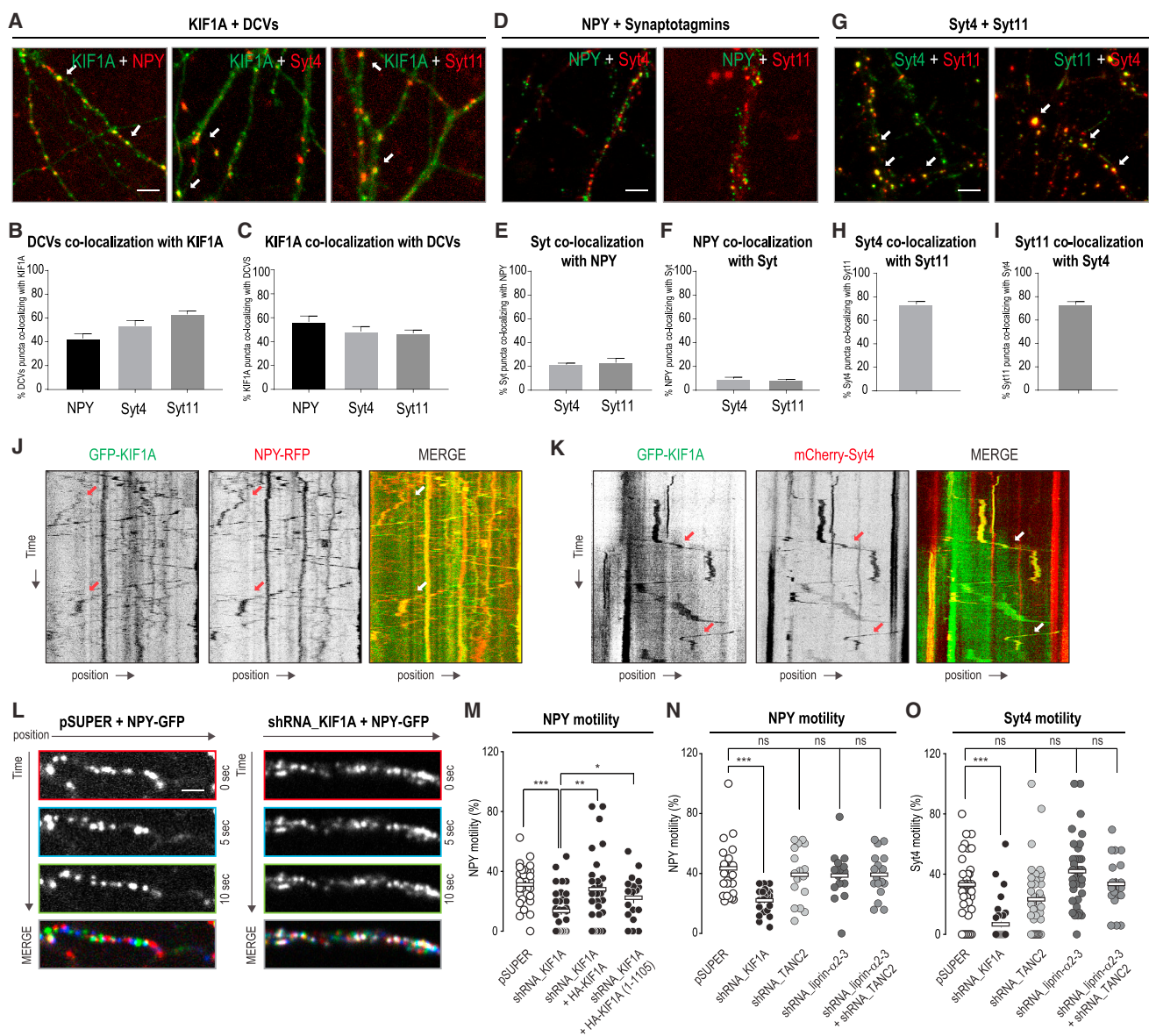
Figure 5. DCV Dendritic Trafficking Is KIF1A Dependent and TANC2/Liprin-α Independent

(A) Neurons (11–14 DIV) co-transfected with GFP-KIF1A (green), in combination with NPY-RFP, mCherry-Syt4, or mCherry-Syt11 (red). Arrows point to co-localizing puncta. Scale bar, 5 μm. See also Figures S3A and S3B.

(B and C) Percentage of co-localizing puncta between DCV proteins and KIF1A (B), and vice versa (C). The bars show mean ± SEM (n = 19–23 dendrites).

(D) NPY-GFP (green), in combination with mCherry-Syt4 or mCherry-Syt11 (red). Scale bar, 5 μm. See also Figures S3C and S3D.

(E and F) Co-localizing puncta between NPY and Syt4 or Syt11 (E), and vice versa (F). The bars show mean ± SEM (n = 21–31 dendrites).

(G) Phluorin-Syt4 (green) with mCherry-Syt11 (red) or Phluorin-Syt11 (green) with mCherry-Syt4 (red). Arrows point to co-localizing puncta. Scale bar, 5 μm. See also Figures S3E and S3F.

(H and I) Co-localizing puncta between Syt4 and Syt11 (H), and vice versa (I). The bars show mean ± SEM (n = 20–27 dendrites).

(J and K) Representative kymographs showing trajectories of NPY-RFP vesicles (J) or mCherry-Syt4 vesicles (K) (red) moving with GFP-KIF1A (green).

(L) Representative images acquired at 10 s intervals showing NPY-GFP motility in dendrites of neurons transfected with pSuper (right) or shRNA_KIF1A (left). In the merged images, red corresponds to 0 s, blue corresponds to 10 s, and green corresponds to 20 s. Scale bar, 5 μm.

(M) Quantification of the percentage of mobile NPY vesicles in neurons (11–14 DIV) co-transfected with NPY-GFP, in combination with pSuper, shRNA_KIF1A, shRNA_KIF1A + FL-HA-KIF1A, or shRNA_KIF1A + HA-KIF1A(1-1105). The bars show mean (n = 18–32 dendrites; *p < 0.05, **p < 0.001, ***p < 0.001, t test).

(N and O) Quantification of the percentage of mobile DCVs in neurons (11–14 DIV) co-transfected with NPY-GFP (N) or mCherry-Syt4 (O), in combination with pSuper, shRNA_KIF1A, shRNA_TANC2, shRNA_liprin-α2-3, or shRNA_liprin-α2-3 + shRNA_TANC2. The bars show mean (n = 17–58 dendrites in N and n = 17–39 dendrites in O; ***p < 0.001, t test). See also Figures S3J–S3L.
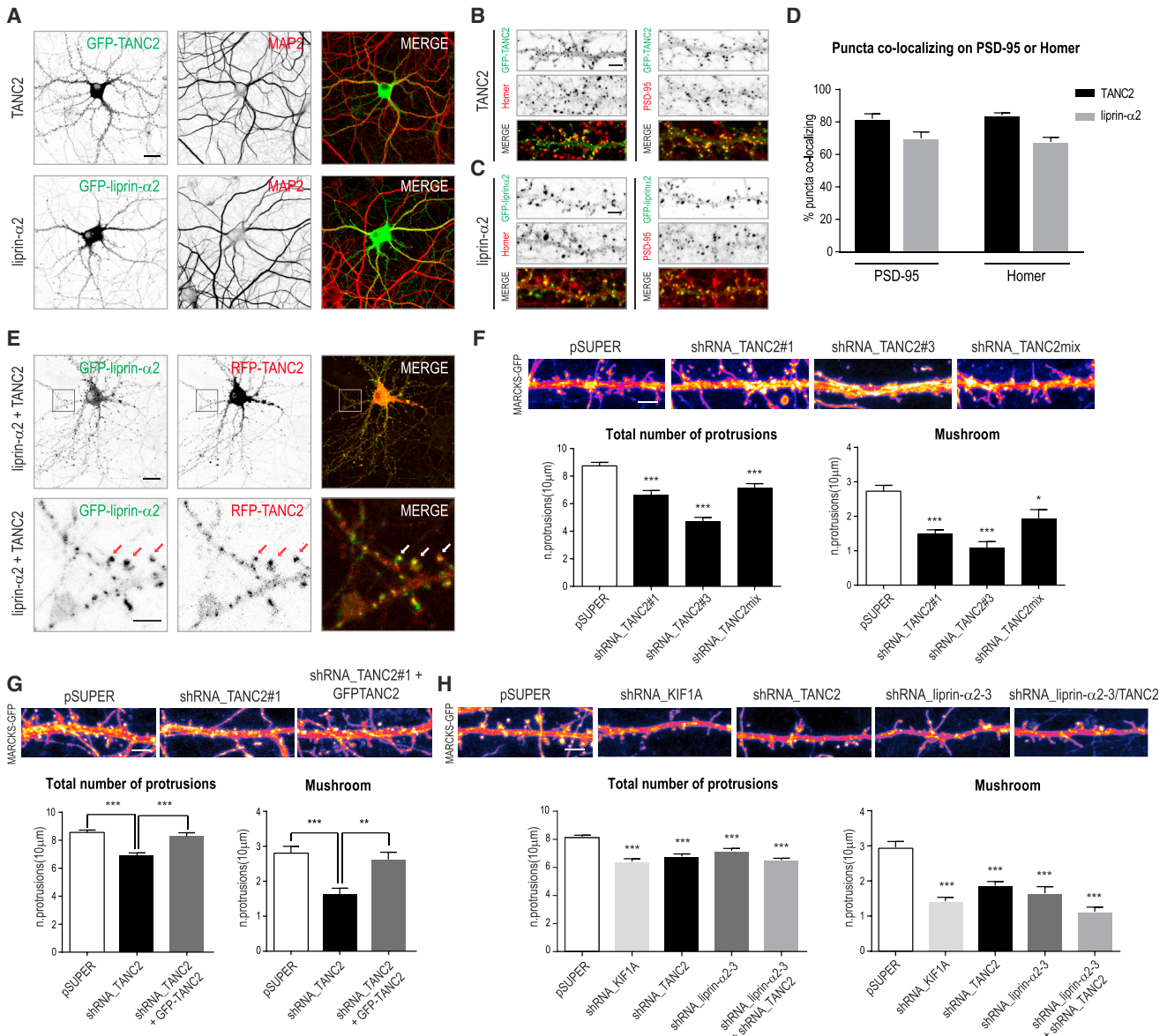
Figure 6. TANC2 and Liprin-α2 Are PSD Scaffolds that Localize in Dendritic Spines

(A) Hippocampal neurons (11–14 DIV) transfected with GFP-TANC2 or GFP-liprin-α2 (green) and stained for MAP2 (red). Scale bar, 20 μm.

(B and C) GFP-TANC2 (B) or GFP-liprin-α2 (C) (green) co-localization with Homer and PSD-95 (red) in dendritic spines. Scale bar, 5 μm.

(D) Quantifications corresponding to the percentage of GFP-TANC2 (B) or GFP-liprin-α2 (C) puncta co-localizing with PSD-95 or Homer. The bars show mean ± SEM (n = 24–36 dendrites).

(E) Neurons co-expressing GFP-liprin-α2 and RFP-TANC2. Scale bar, 20 μm. Bottom panels correspond to higher magnification showing TANC2 and liprin-α2 co-localization in dendritic spines. Arrows point to co-localizing puncta. Scale bar, 5 μm.

(F) Dendritic protrusions of pSuper or TANC2-KD (knockdown) neurons (shRNA_TANC2#1, shRNA_TANC2#3, and shRNA_TANC2mix) co-transfected with MARCKS-GFP to visualize membrane morphology. Scale bar, 5 μm. Graphs show quantifications of protrusion density (number of protrusions per 10 μm) for total number of protrusions (left) or mushroom-shaped protrusions (right). The bars show mean ± SEM (n = 30–33 dendrites; *p < 0.05, ***p < 0.001, t test).

(G) Dendritic protrusions in neurons co-transfected with pSuper, shRNA_TANC2#1, or shRNA_TANC2#1 + GFP-TANC2, in combination with MARCKS-GFP. Scale bar, 5 μm. The bars show mean ± SEM (n = 54–75 dendrites, **p < 0.01, ***p < 0.001, t test).

(H) Dendritic protrusions in neurons transfected with pSuper, shRNA_KIF1A, shRNA_TANC2, shRNA_liprin-α2-3, or shRNA_liprin-α2-3 + shRNA_TANC2, together with MARCKS-GFP. Scale bar, 5 μm. The bars show mean ± SEM (n = 30–36 dendrites, ***p < 0.001, t test).
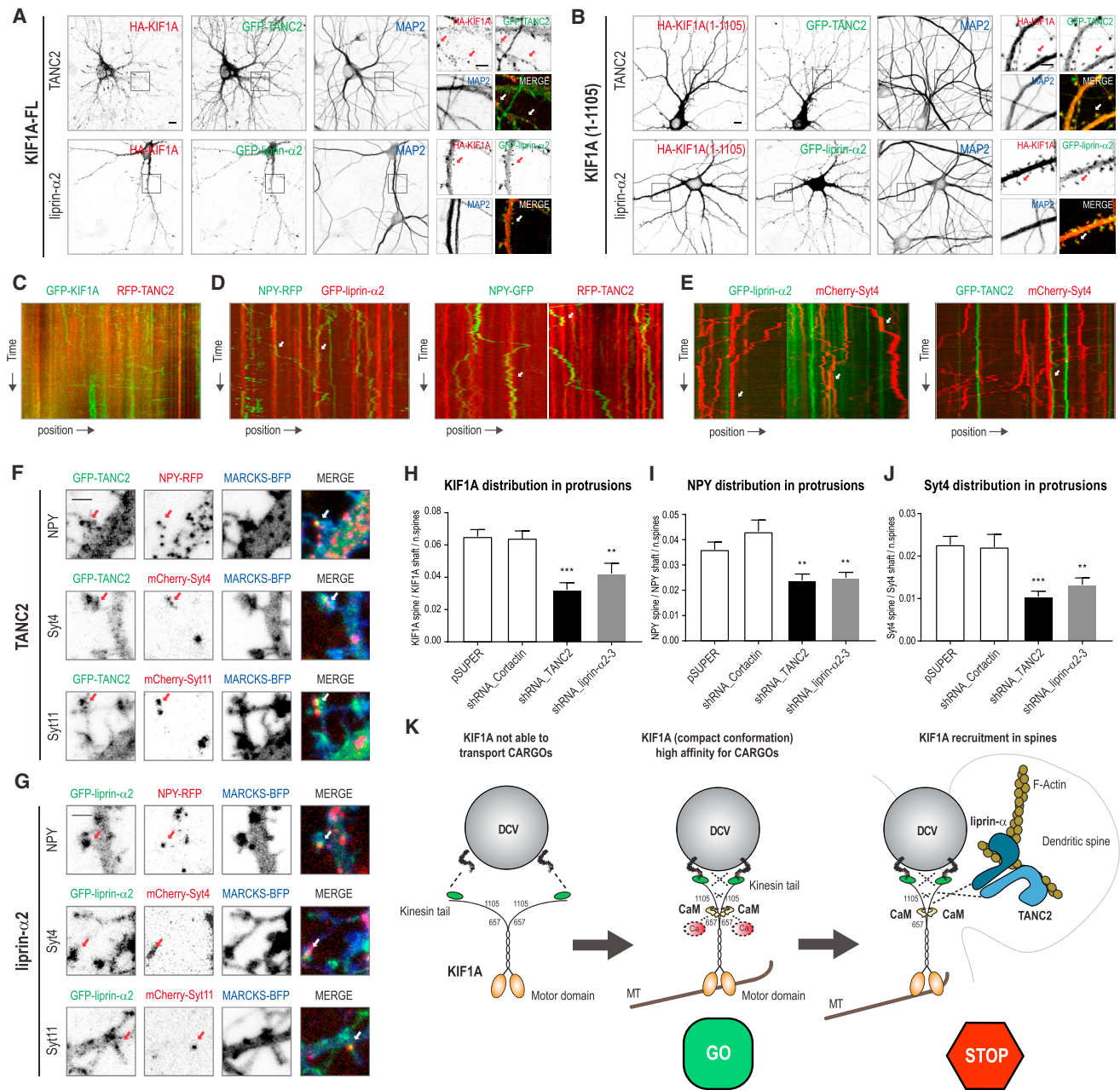
Figure 7. TANC2 and Liprin-α Recruit KIF1A-Driven DCVs in Dendritic Spines

(A and B) Neurons co-expressing GFP-TANC2 or GFP-liprin-α2 (green), in combination with HA-KIF1A (A) or HA-KIF1A(1-1105) (B) (red) and stained for MAP2 (blue). Scale bar, 10 μm. Panels on the right correspond to higher magnifications showing dendritic TANC2 and liprin-α2 puncta co-localizing with KIF1A. Scale bar, 5 μm.

(C) Kymographs showing trajectories of GFP-KIF1A and RFP-TANC2 in a selected dendritic region of transfected hippocampal neurons (11–14 DIV).

(D) Trajectories of NPY-RFP (green) vesicles pausing at GFP-liprin-α2 (red) clusters (left panel); trajectories of NPY-GFP (green) vesicles pausing at RFP-TANC2 (red) clusters (right panel).

(E) mCherry-Syt4 (red) vesicles pausing at GFP-liprin-α2 (green) clusters (left panel) or at GFP-TANC2 (green) clusters (right panel).

(F and G) GFP-TANC2 (F) or GFP-liprin-α2 (G) co-localizing with NPY-RFP, mCherry-Syt4, or mCherry-Syt11 puncta in dendritic protrusions visualized with MARCKS-BFP. Scale bar, 2 μm.

(H–J) Quantifications showing the percentage of GFP-KIF1A (H), NPY-GFP (I), and mCherry-Syt4 (J) puncta in dendritic protrusions, measured in neurons transfected with pSuper, shRNA_Cortactin, shRNA_TANC2, and shRNA_liprin-α2-3 (11–14 DIV) and filled with MARCKS-BFP. The bars show mean ± SEM (n = 30–57 dendrites in H, n = 35–71 dendrites in I, and n = 43–90 dendrites in J; *p < 0.05, **p < 0.01, ***p < 0.001, t test).

(legend continued on next page)

TANC2 Disease Mutations Abolish the Interaction with KIF1A and Affect KIF1A-DCV Recruitment

The preceding findings on the role of TANC2 in DCV transport turned our interest into potential consequences for neuronal dysfunction. TANC2 gene mutations R760C and R1066X (nonsense mutation) were found in patients with intellectual disorders and autism spectrum disorder, respectively (de Ligt et al., 2012; Iossifov et al., 2012). In the last part, we wanted to test whether those mutants may be affecting TANC2 localization to dendritic spines and/or its ability to bind KIF1A. While the localization of TANC2-R760C was similar to the WT TANC2, TANC2-R1066X failed to accumulate at the dendritic spines (Figures S6A and S6B). These results are in agreement with an important role of the C-terminal PDZ binding domain for TANC2 synaptic localization (Figure S4A). Furthermore, AP-WB experiments revealed strongly reduced binding between both TANC2 mutants and KIF1A (Figure S6C).

To directly assess the effect of TANC2 point mutation (R760C) on KIF1A and DCV transport, we next produced chimeric proteins, which are the result of the fusion between NF186 (Neurofascin) and TANC2(1-832_WT) or TANC2(1-832_R760C). As expected, both Neurofascin-fusion proteins mis-accumulate TANC2 at the AIS (Figures S6D and S6E). Neurons co-expressing a WT TANC2 chimera showed reduced run length (Figure S6F), speed (Figure S6G), and run duration (Figure S6H) of anterograde-transported DCVs at the AIS compared to a control NF186, whereas in the presence of a mutant R760C, DCV motility was not affected (Figures S6F–S6H). These data suggest that a single point mutation (within the N-terminal part of TANC2) found in patients with intellectual disorders, apart from being detrimental for binding with KIF1A (Figure S6C), drastically impairs the recruitment of KIF1A-transported vesicles in neurons. Altogether, these data suggest that the aberrant localization, the abolished interaction with KIF1A, and the deficient recruitment of KIF1A-driven vesicles of TANC2 mutants may contribute to the underlying molecular mechanisms that lead to neurological defects observed in patients.

DISCUSSION

Ca^{2+}/CaM Interacts with KIF1A and Allows DCV Binding and Motility

In neurons, calcium is a regulatory factor for multiple elements of the trafficking machinery. Calcium and calcium-activated proteins control motor protein processivity and motor-cargo binding (Hirokawa et al., 2010; Schlager and Hoogenraad, 2009). For example, Ca^{2+}/CaM allows activation of actin-based motors, such as myosin Va (Krementsov et al., 2004), myosin VI (Batters et al., 2016), and myosin 1C (Lu et al., 2015). In those cases, calcium is required for an initial activation of the myosin motor protein, allowing the transition from a backfolded conformation to an active status. Another example is the activation of Ca^{2+}/CaM-dependent protein kinase II (CaMKII) by calcium, which in turn

phosphorylates KIF17, leading to the release of NMDA receptor-containing vesicles (Guillaud et al., 2008). Finally, the regulation of mitochondrial trafficking depends on calcium. Upon calcium binding, the adaptor protein Miro interacts with the motor domain of KIF5 motors, thereby preventing its microtubule interaction and inhibiting the transport of mitochondria (Macaskill et al., 2009; Wang and Schwarz, 2009). Similar to this mechanism, cytoplasmic KIF1A is in an auto-inhibited state and becomes active only upon cargo binding (Hammond et al., 2009; Niwa et al., 2016). In this study, we were able to decipher the role of calcium in KIF1A-dependent vesicle trafficking. We show that Ca^{2+}/CaM-dependent modulation on KIF1A allows for binding to vesicular cargo. Our results indicate that at low calcium concentrations, the tail domain of KIF1A does not bind to vesicular cargo, whereas at high calcium concentrations, CaM binds KIF1A, allowing for subsequent DCV motility. Thus, we propose a mechanism in which Ca^{2+}/CaM regulates the loading of DCVs. This model potentially represents a more general paradigm for other kinesins and cargoes in response to calcium. For example, KIF1Bβ contains a predicted CaM binding site in a highly conserved region and therefore could undergo similar Ca^{2+}/CaM-dependent dynamics.

TANC2 and Liprin-α Capture KIF1A-Driven DCVs

Syt4 is present on DCVs and is transported by KIF1A along microtubules in the dendritic shaft (Arthur et al., 2010). Microtubule entry into dendritic spines was proposed as a mechanism of local delivery of KIF1A-mediated DCVs (McVicker et al., 2016). Our data point to two scaffolding proteins, TANC2 and liprin-α, present in dendritic spines as important players in the mechanism behind KIF1A-transported DCV capture. First, TANC2 and liprin-α bind the stalk domain of KIF1A. Second, they are stably present in dendritic spines while not being part of the KIF1A-cargo complex. Third, although TANC2 and liprin-α do not directly affect the motility of KIF1A-transported DCVs, they influence the cargo distribution in dendritic spines. Based on those points, we speculate that TANC2 and liprin-α, interacting with KIF1A, are able to stop and capture KIF1A-bound DCVs upon dendritic spine entry. In this model, TANC2 and liprin-α act as local signposts tethering KIF1A-transported DCVs. Consistent with our model, neurons lacking KIF1A show spine morphology defects, which can be directly caused by an altered transport of DCVs within the dendritic spines. In this study, we focused on KIF1A-dependent DCV transport in dendrites; however, the same general principles might be applied to the transport of SVs in the axonal compartment. Similar mechanisms have been described at the pre-synaptic axonal boutons, where static clusters of liprin-α can capture KIF1A-transported SVs (Olsen et al., 2005; Wu et al., 2013, 2016) or where actin pre-synaptic pools locally recruit DCVs (Bharat et al., 2017). Based on our biochemical results, DCV recruitment is favored by low calcium concentrations, thereby working as an opposing mechanism counteracting the Ca^{2+}/CaM-induced DCV mobility. Myosin

(K) Hypothetical model of KIF1A-dependent transport of DCVs in dendritic spines. KIF1A, in low Ca^{2+}, is in an auto-inhibited conformation, unable to efficiently bind any cargo. In the presence of high Ca^{2+}, KIF1A interacts with CaM, resulting in a conformational change of its C-terminal tail. Upon Ca^{2+}/CaM binding, KIF1A is activated, allowing for DCV loading and motility. KIF1A-driven DCVs are recruited in dendritic spines by liprin-α and TANC2, which ensure a precise mechanism of synaptic tagging for the vesicles.

motors may play an additional role in trafficking DCVs into spines. Specifically, it was proposed that myosin V modulates DCV transport and delivery (Bittins et al., 2010) and myosin V activity is regulated by a similar Ca^{2+}/CaM mechanism (Lu et al., 2006; Nguyen and Higuchi, 2005). Thus, local Ca^{2+} concentrations have an important role in the modulation of DCV trafficking and delivery in and out of dendritic spines.

In summary, we propose that Ca^{2+}/CaM regulates cargo pick-up and scaffolding proteins liprin-α and TANC2 recruit KIF1A-driven DCVs into spines. Our findings reveal a potential general mechanism that depends on two basic elements: calcium to load motors to cargo and specific signposts to unload cargo. Given that alterations in cargo trafficking pathways were described in several neurological diseases, our findings that some TANC2 disease mutants do not interact with KIF1A are bringing to light additional molecular targets to investigate the trafficking machinery in neuropathological disease models.

EXPERIMENTAL PROCEDURES

Animals
All experiments were approved by the DEC Dutch Animal Experiments Committee (Dier Experimenten Commissie), performed in line with institutional guidelines of Utrecht University, and conducted in agreement with Dutch law (1996 Wet op de Dierproeven) and European regulations (Directive 2010/63/EU). For details, see Supplemental Experimental Procedures. Female pregnant Wister rats were obtained from Janvier Laboratories. Hippocampal neurons were obtained from embryos of both genders at the embryonic day 18 (E18) stage of development.

Expression Vectors and shRNA Constructs
pebioGFP-KIF1A(657-1105, 657-1698) correspond to truncated versions of the KIF1A rat variant 2 (XM_003750741). HA-TANC2 and GFP-TANC2 were generated using FLAG-TANC2 as a template, as described in Han et al. (2010). The following shRNA sequences are used in this study: TANC2#1 (5′-CCTCAGTCAAGGGTCATAT-3′) targeting rat TANC2 mRNA (XM_008768351.1), shRNA_KIF1A (Kevenaar et al., 2016), and shRNA_liprin-α2/α3 (Spangler et al., 2013). All other constructs were created using PCR-based strategies. For details, see Supplemental Experimental Procedures.

Hippocampal Neuron Cultures, Transfections, and Treatments
Primary hippocampal cultures were prepared from E18 rat brains. Cells were plated on coverslips coated with poly-L-lysine (30 μg/mL) and laminin (2 μg/mL) at a density of 100,000/well. Hippocampal neurons were transfected using lipofectamine (Invitrogen). Neuron cultures were treated with 10 μM latrunculin B, 10 μM jasplakinolide, 10 μM BAPTA-AM, or 40 μM bicuculline and fixed or imaged from 0 to 1 hr after addition of the drugs. For details, see Supplemental Experimental Procedures.

AP-MS Using Biotin or GFP Pull-Down on Rat Brain Extracts
Brains were obtained from female adult rats and homogenized in tissue lysis buffer (50 mM Tris HCl, 150 mM NaCl, 0.1% SDS, 0.2% NP-40, and protease inhibitors). Brain lysates were centrifuged at 16,000 × g for 15 min at 4°C, and the supernatant was then incubated for 1 hr at 4°C with beads previously conjugated with the protein of interest. For details, see Supplemental Experimental Procedures.

Sample Preparation, Peptide Fractionation, MS, and Data Analysis
All samples were analyzed on an electron transfer dissociation (ETD)-enabled LTQ-Orbitrap Elite coupled to Proxeon EASY-nLC 1000 (Thermo Fisher Scientific) or on an Orbitrap Q-Exactive mass spectrometer (Thermo Fisher Scientific) coupled to an Agilent 1290 Infinity LC (Agilent Technologies). The full MS methods are available in the Supplemental Experimental Procedures.

Live-Cell Imaging Microscopy and Analysis
Live-cell imaging experiments were performed in an inverted spinning disk confocal microscope equipped with a Plan Apo VC 100×/60× NA 1.40 oil objective and an incubation chamber mounted on a motorized XYZ stage, which were all controlled using MetaMorph (Molecular Devices) software. For details, see Supplemental Experimental Procedures.

Statistical Methods
AP-MS data were analyzed using the SAINT (Significance Analysis of INTeractions, v.2.3.2) algorithm. Statistical significance was determined using Student's t test assuming a two-tailed variation. The graphs represent mean ± SEM. For details, see Supplemental Experimental Procedures.

DATA AND SOFTWARE AVAILABILITY

The accession number for the mass spectrometry proteomic data reported in this paper is PRIDE: PXD010080.

SUPPLEMENTAL INFORMATION

Supplemental Information includes Supplemental Experimental Procedures, six figures, and four tables and can be found with this article online at https://doi.org/10.1016/j.celrep.2018.06.071.

AUTHOR CONTRIBUTIONS

R.S. cloned the constructs; designed and performed proteomic, biochemical, and imaging experiments; and analyzed the data; G.P. and E.E.Z. conducted live imaging experiments and analyzed the data; J.H. and I.G.S.J. cloned DNA constructs and performed biochemical and imaging experiments; O.K. performed XL-MS experiments; R.A.S. supervised the XL-MS part; A.F.M.A. supervised the proteomic part; R.S. designed and assembled the figures; R.S. and C.C.H. wrote the manuscript with input from G.P.; and C.C.H. supervised and coordinated the study.

DECLARATION OF INTERESTS

The authors declare no competing interests.

REFERENCES

Arthur, C.P., Dean, C., Pagratis, M., Chapman, E.R., and Stowell, M.H. (2010). Loss of synaptotagmin IV results in a reduction in synaptic vesicles and a distortion of the Golgi structure in cultured hippocampal neurons. Neuroscience 167, 135–142.

Barkus, R.V., Klyachko, O., Horiuchi, D., Dickson, B.J., and Saxton, W.M. (2008). Identification of an axonal kinesin-3 motor for fast anterograde vesicle transport that facilitates retrograde transport of neuropeptides. Mol. Biol. Cell 19, 274–283.

Batters, C., Brack, D., Ellrich, H., Averbeck, B., and Veigel, C. (2016). Calcium can mobilize and activate myosin-VI. Proc. Natl. Acad. Sci. USA 113, E1162–E1169.

Bharat, V., Siebrecht, M., Burk, K., Ahmed, S., Reissner, C., Kohansal-Nodehi, M., Steubler, V., Zweckstetter, M., Ting, J.T., and Dean, C. (2017). Capture of dense core vesicles at synapses by JNK-dependent phosphorylation of synaptotagmin-4. Cell Rep. 21, 2118–2133.

Bittins, C.M., Eichler, T.W., Hammer, J.A., 3rd, and Gerdes, H.H. (2010). Dominant-negative myosin Va impairs retrograde but not anterograde axonal transport of large dense core vesicles. Cell. Mol. Neurobiol. 30, 369–379.

Choi, H., Larsen, B., Lin, Z.Y., Breitkreutz, A., Mellacheruvu, D., Fermin, D., Qin, Z.S., Tyers, M., Gingras, A.C., and Nesvizhskii, A.I. (2011). SAINT: probabilistic scoring of affinity purification-mass spectrometry data. Nat. Methods 8, 70–73.

de Ligt, J., Willemsen, M.H., van Bon, B.W., Kleefstra, T., Yntema, H.G., Kroes, T., Vulto-van Silfhout, A.T., Koolen, D.A., de Vries, P., Gilissen, C., et al. (2012). Diagnostic exome sequencing in persons with severe intellectual disability. N. Engl. J. Med. 367, 1921–1929.

de Wit, J., Toonen, R.F., Verhaagen, J., and Verhage, M. (2006). Vesicular trafficking of semaphorin 3A is activity-dependent and differs between axons and dendrites. Traffic 7, 1060–1077.

Dean, C., Liu, H., Dunning, F.M., Chang, P.Y., Jackson, M.B., and Chapman, E.R. (2009). Synaptotagmin-IV modulates synaptic function and long-term potentiation by regulating BDNF release. Nat. Neurosci. 12, 767–776.

Esteves da Silva, M., Adrian, M., Schätzle, P., Lipka, J., Watanabe, T., Cho, S., Futai, K., Wierenga, C.J., Kapitein, L.C., and Hoogenraad, C.C. (2015). Positioning of AMPA receptor-containing endosomes regulates synapse architecture. Cell Rep. 13, 933–943.

Fromer, M., Pocklington, A.J., Kavanagh, D.H., Williams, H.J., Dwyer, S., Gormley, P., Georgieva, L., Rees, E., Palta, P., Ruderfer, D.M., et al. (2014). De novo mutations in schizophrenia implicate synaptic networks. Nature 506, 179–184.

Gasparini, A., Tosatto, S.C.E., Murgia, A., and Leonardi, E. (2017). Dynamic scaffolds for neuronal signaling: in silico analysis of the TANC protein family. Sci. Rep. 7, 6829.

Guillaud, L., Wong, R., and Hirokawa, N. (2008). Disruption of KIF17-Mint1 interaction by CaMKII-dependent phosphorylation: a molecular model of kinesin-cargo release. Nat. Cell Biol. 10, 19–29.

Gumy, L.F., Katrukha, E.A., Grigoriev, I., Jaarsma, D., Kapitein, L.C., Akhmanova, A., and Hoogenraad, C.C. (2017). MAP2 defines a pre-axonal filtering zone to regulate KIF1- versus KIF5-dependent cargo transport in sensory neurons. Neuron 94, 347–362.

Hammond, J.W., Cai, D., Blasius, T.L., Li, Z., Jiang, Y., Jih, G.T., Meyhofer, E., and Verhey, K.J. (2009). Mammalian kinesin-3 motors are dimeric in vivo and move by processive motility upon release of autoinhibition. PLoS Biol. 7, e72.

Han, S., Nam, J., Li, Y., Kim, S., Cho, S.H., Cho, Y.S., Choi, S.Y., Choi, J., Han, K., Kim, Y., et al. (2010). Regulation of dendritic spines, spatial memory, and embryonic development by the TANC family of PSD-95-interacting proteins. J. Neurosci. 30, 15102–15112.

Hanada, T., Lin, L., Tibaldi, E.V., Reinherz, E.L., and Chishti, A.H. (2000). GAKIN, a novel kinesin-like protein associates with the human homologue of the Drosophila discs large tumor suppressor in T lymphocytes. J. Biol. Chem. 275, 28774–28784.

Hirokawa, N., Niwa, S., and Tanaka, Y. (2010). Molecular motors in neurons: transport mechanisms and roles in brain function, development, and disease. Neuron 68, 610–638.

Iossifov, I., Ronemus, M., Levy, D., Wang, Z., Hakker, I., Rosenbaum, J., Yamrom, B., Lee, Y.H., Narzisi, G., Leotta, A., et al. (2012). De novo gene disruptions in children on the autistic spectrum. Neuron 74, 285–299.

Kapitein, L.C., Schlager, M.A., Kuijpers, M., Wulf, P.S., van Sponsen, M., MacKintosh, F.C., and Hoogenraad, C.C. (2010). Mixed microtubules steer dynein-driven cargo transport into dendrites. Curr. Biol. 20, 290–299.

Kevenaar, J.T., Bianchi, S., van Sponsen, M., Olieric, N., Lipka, J., Frias, C.P., Mikhaylova, M., Harterink, M., Keijzer, N., Wulf, P.S., et al. (2016). Kinesin-binding protein controls microtubule dynamics and cargo trafficking by regulating kinesin motor activity. Curr. Biol. 26, 849–861.

Klopfenstein, D.R., Tomishige, M., Stuurman, N., and Vale, R.D. (2002). Role of phosphatidylinositol(4,5)bisphosphate organization in membrane transport by the Unc104 kinesin motor. Cell 109, 347–358.

Krementsov, D.N., Krementsova, E.B., and Trybus, K.M. (2004). Myosin V: regulation by calcium, calmodulin, and the tail domain. J. Cell Biol. 164, 877–886.

Leterrier, C., and Dargent, B. (2014). No Pasaran! Role of the axon initial segment in the regulation of protein transport and the maintenance of axonal identity. Semin. Cell Dev. Biol. 27, 44–51.

Li, Z., and Sacks, D.B. (2003). Elucidation of the interaction of calmodulin with the IQ motifs of IQGAP1. J. Biol. Chem. 278, 4347–4352.

Lipka, J., Kapitein, L.C., Jaworski, J., and Hoogenraad, C.C. (2016). Microtubule-binding protein doublecortin-like kinase 1 (DCLK1) guides kinesin-3-mediated cargo transport to dendrites. EMBO J. 35, 302–318.

Lo, K.Y., Kuzmin, A., Unger, S.M., Petersen, J.D., and Silverman, M.A. (2011). KIF1A is the primary anterograde motor protein required for the axonal transport of dense-core vesicles in cultured hippocampal neurons. Neurosci. Lett. 491, 168–173.

Lochner, J.E., Spangler, E., Chavarha, M., Jacobs, C., McAllister, K., Schuttner, L.C., and Scalettar, B.A. (2008). Efficient copackaging and cotransport yields postsynaptic colocalization of neuromodulators associated with synaptic plasticity. Dev. Neurobiol. 68, 1243–1256.

Lu, H., Krementsova, E.B., and Trybus, K.M. (2006). Regulation of myosin V processivity by calcium at the single molecule level. J. Biol. Chem. 281, 31987–31994.

Lu, Q., Li, J., Ye, F., and Zhang, M. (2015). Structure of myosin-1c tail bound to calmodulin provides insights into calcium-mediated conformational coupling. Nat. Struct. Mol. Biol. 22, 81–88.

Macaskill, A.F., Rinholm, J.E., Twelvetrees, A.E., Arancibia-Carcamo, I.L., Muir, J., Fransson, A., Aspenstrom, P., Attwell, D., and Kittler, J.T. (2009). Miro1 is a calcium sensor for glutamate receptor-dependent localization of mitochondria at synapses. Neuron 61, 541–555.

Maeder, C.I., Shen, K., and Hoogenraad, C.C. (2014). Axon and dendritic trafficking. Curr. Opin. Neurobiol. 27, 165–170.

McVicker, D.P., Awe, A.M., Richters, K.E., Wilson, R.L., Cowdrey, D.A., Hu, X., Chapman, E.R., and Dent, E.W. (2016). Transport of a kinesin-cargo pair along microtubules into dendritic spines undergoing synaptic plasticity. Nat. Commun. 7, 12741.

Millecamps, S., and Julien, J.P. (2013). Axonal transport deficits and neurodegenerative diseases. Nat. Rev. Neurosci. 14, 161–176.

Miller, K.E., DeProto, J., Kaufmann, N., Patel, B.N., Duckworth, A., and Van Vactor, D. (2005). Direct observation demonstrates that Liprin-alpha is required for trafficking of synaptic vesicles. Curr. Biol. 15, 684–689.

Mruk, K., Farley, B.M., Ritacco, A.W., and Kobertz, W.R. (2014). Calmodulation meta-analysis: predicting calmodulin binding via canonical motif clustering. J. Gen. Physiol. 144, 105–114.

Nguyen, H., and Higuchi, H. (2005). Motility of myosin V regulated by the dissociation of single calmodulin. Nat. Struct. Mol. Biol. 12, 127–132.

Niwa, S., Tanaka, Y., and Hirokawa, N. (2008). KIF1Bbeta- and KIF1A-mediated axonal transport of presynaptic regulator Rab3 occurs in a GTP-dependent manner through DENN/MADD. Nat. Cell Biol. 10, 1269–1279.

Niwa, S., Lipton, D.M., Morikawa, M., Zhao, C., Hirokawa, N., Lu, H., and Shen, K. (2016). Autoinhibition of a neuronal kinesin UNC-104/KIF1A regulates the size and density of synapses. Cell Rep. 16, 2129–2141.

Okada, Y., Yamazaki, H., Sekine-Aizawa, Y., and Hirokawa, N. (1995). The neuron-specific kinesin superfamily protein KIF1A is a unique monomeric motor for anterograde axonal transport of synaptic vesicle precursors. Cell 81, 769–780.

Olsen, O., Moore, K.A., Fukata, M., Kazuta, T., Trinidad, J.C., Kauer, F.W., Streuli, M., Misawa, H., Burlingame, A.L., Nicoll, R.A., and Bredt, D.S. (2005). Neurotransmitter release regulated by a MALS-liprin-alpha presynaptic complex. J. Cell Biol. *170*, 1127–1134.

Schlager, M.A., and Hoogenraad, C.C. (2009). Basic mechanisms for recognition and transport of synaptic cargos. Mol. Brain *2*, 25.

Shin, H., Wyszynski, M., Huh, K.H., Valtschanoff, J.G., Lee, J.R., Ko, J., Streuli, M., Weinberg, R.J., Sheng, M., and Kim, E. (2003). Association of the kinesin motor KIF1A with the multimodular protein liprin-alpha. J. Biol. Chem. *278*, 11393–11401.

Sieburth, D., Ch'ng, Q., Dybbs, M., Tavazoie, M., Kennedy, S., Wang, D., Dupuy, D., Rual, J.F., Hill, D.E., Vidal, M., et al. (2005). Systematic analysis of genes required for synapse structure and function. Nature *436*, 510–517.

Sirajuddin, M., Rice, L.M., and Vale, R.D. (2014). Regulation of microtubule motors by tubulin isotypes and post-translational modifications. Nat. Cell Biol. *16*, 335–344.

Spangler, S.A., Schmitz, S.K., Kevenaar, J.T., de Graaff, E., de Wit, H., Demmers, J., Toonen, R.F., and Hoogenraad, C.C. (2013). Liprin-α2 promotes the presynaptic recruitment and turnover of RIM1/CASK to facilitate synaptic transmission. J. Cell Biol. *201*, 915–928.

Wagner, O.I., Esposito, A., Köhler, B., Chen, C.W., Shen, C.P., Wu, G.H., Butkevich, E., Mandalapu, S., Wenzel, D., Wouters, F.S., and Klopfenstein, D.R. (2009). Synaptic scaffolding protein SYD-2 clusters and activates kinesin-3 UNC-104 in *C. elegans*. Proc. Natl. Acad. Sci. USA *106*, 19605–19610.

Wang, X., and Schwarz, T.L. (2009). The mechanism of Ca2+ -dependent regulation of kinesin-mediated mitochondrial motility. Cell *136*, 163–174.

Wu, Y.E., Huo, L., Maeder, C.I., Feng, W., and Shen, K. (2013). The balance between capture and dissociation of presynaptic proteins controls the spatial distribution of synapses. Neuron *78*, 994–1011.

Wu, G.H., Muthaiyan Shanmugam, M., Bhan, P., Huang, Y.H., and Wagner, O.I. (2016). Identification and characterization of LIN-2(CASK) as a regulator of kinesin-3 UNC-104(KIF1A) motility and clustering in neurons. Traffic *17*, 891–907.

Wyszynski, M., Kim, E., Dunah, A.W., Passafaro, M., Valtschanoff, J.G., Serra-Pagès, C., Streuli, M., Weinberg, R.J., and Sheng, M. (2002). Interaction between GRIP and liprin-alpha/SYD2 is required for AMPA receptor targeting. Neuron *34*, 39–52.

Yamada, K.H., Hanada, T., and Chishti, A.H. (2007). The effector domain of human Dlg tumor suppressor acts as a switch that relieves autoinhibition of kinesin-3 motor GAKIN/KIF13B. Biochemistry *46*, 10039–10045.

Yamniuk, A.P., and Vogel, H.J. (2004). Calmodulin's flexibility allows for promiscuity in its interactions with target proteins and peptides. Mol. Biotechnol. *27*, 33–57.

Yap, K.L., Kim, J., Truong, K., Sherman, M., Yuan, T., and Ikura, M. (2000). Calmodulin target database. J. Struct. Funct. Genomics *1*, 8–14.

Yogev, S., Cooper, R., Fetter, R., Horowitz, M., and Shen, K. (2016). Microtubule organization determines axonal transport dynamics. Neuron *92*, 449–460.

Zahn, T.R., Angleson, J.K., MacMorris, M.A., Domke, E., Hutton, J.F., Schwartz, C., and Hutton, J.C. (2004). Dense core vesicle dynamics in *Caenorhabditis elegans* neurons and the role of kinesin UNC-104. Traffic *5*, 544–559.

Zhang, M., Tanaka, T., and Ikura, M. (1995). Calcium-induced conformational transition revealed by the solution structure of apo calmodulin. Nat. Struct. Biol. *2*, 758–767.

Zhu, J., Shang, Y., Xia, Y., Zhang, R., and Zhang, M. (2016). An atypical MAGUK GK target recognition mode revealed by the interaction between DLG and KIF13B. Structure *24*, 1876–1885.

Supplemental Information

Regulation of KIF1A-Driven Dense Core Vesicle

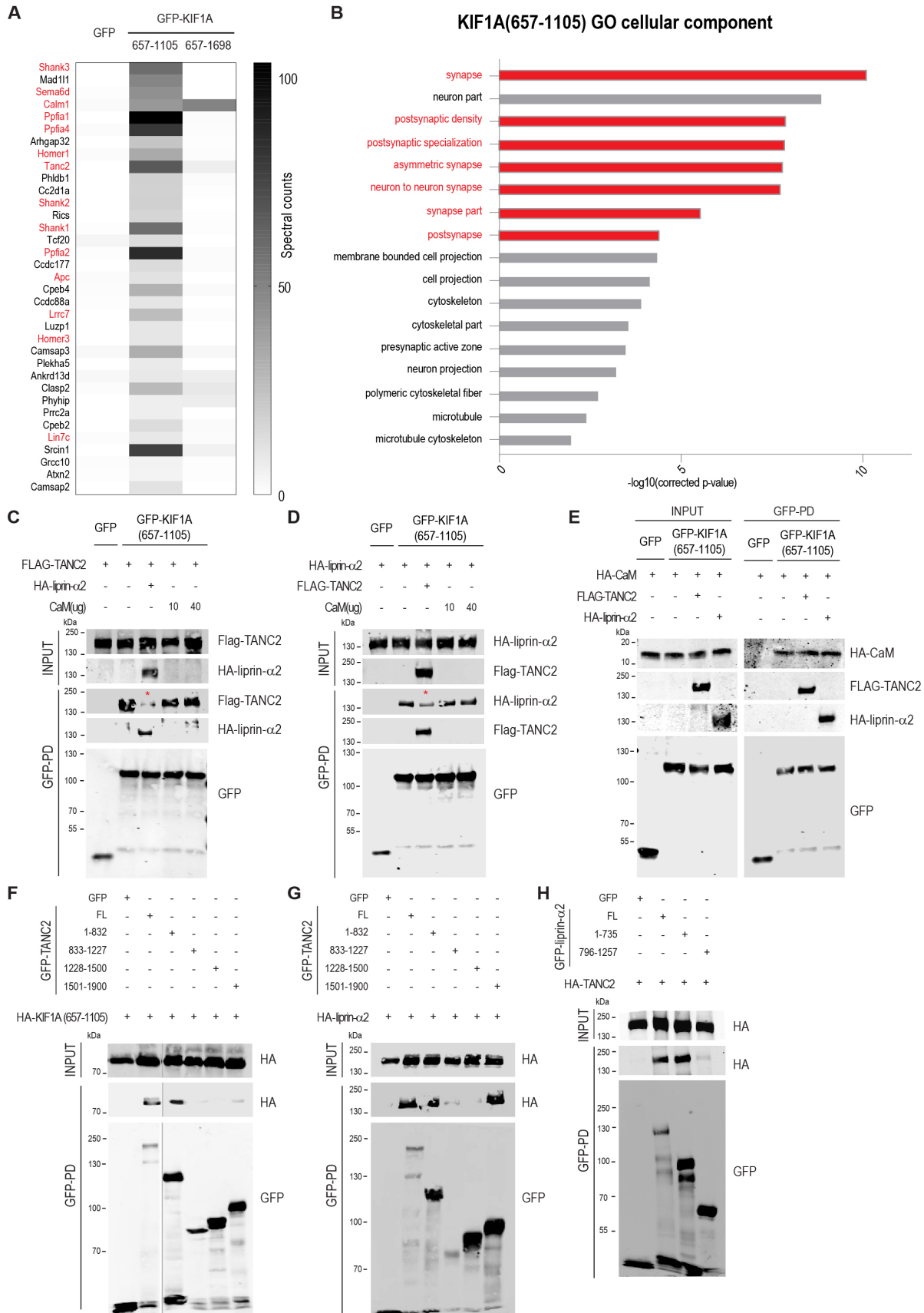## Transport: Ca^{2+}/CaM Controls DCV Binding and

Liprin-α/TANC2 Recruits DCVs to Postsynaptic Sites

Riccardo Stucchi, Gabriela Plucińska, Jessica J.A. Hummel, Eitan E. Zahavi, Irune Guerra San Juan, Oleg Klykov, Richard A. Scheltema, A.F. Maarten Altelaar, and Casper C. Hoogenraad

SUPPLEMENTAL FIGURES

Figure S1

A — Heatmap of spectral counts for GFP, GFP-KIF1A (657-1105), and GFP-KIF1A (657-1698) pull-downs. Proteins listed: Shank3, Mad1l1, Sema6d, Calm1, Ppfia1, Ppfia4, Arhgap32, Homer1, Tanc2, Phldb1, Cc2d1a, Shank2, Rics, Shank1, Tcf20, Ppfia2, Ccdc177, Apc, Cpeb4, Ccdc88a, Lrrc7, Luzp1, Homer3, Camsap3, Plekha5, Ankrd13d, Clasp2, Phyhip, Prrc2a, Cpeb2, Lin7c, Srcin1, Grcc10, Atxn2, Camsap2.

B — KIF1A(657-1105) GO cellular component: synapse, neuron part, postsynaptic density, postsynaptic specialization, asymmetric synapse, neuron to neuron synapse, synapse part, postsynapse, membrane bounded cell projection, cell projection, cytoskeleton, cytoskeletal part, presynaptic active zone, neuron projection, polymeric cytoskeletal fiber, microtubule, microtubule cytoskeleton. X-axis: -log10(corrected p-value).

Figure S1. Related to Figure 1. KIF1A(657-1105) interacts with TANC2, liprin-α2, CaM and shows high binding affinity for a restricted group of post synaptic density (PSD) proteins

(A) List of KIF1A (657-1105) interactors identified by LC/MS-MS in rat brain affinity purification (AP) experiments. BioGFP-CTR and bioGFP-KIF1A truncated isoforms (657-1105; 657-1698) were firstly expressed in HEK293 cells, purified using streptavidin-pulldowns and then incubated with rat brain extracts. Candidate proteins identified by MS are considered true KIF1A(657-1105) interactors when their probability >0.98 using the SAINT algorithm. Heat map shows total spectral counts detected for each protein candidate in AP-MS experiments of bioGFP, bioGFP-KIF1A(657-1105) or bioGFP-KIF1A(657-1698). Selected candidates shown in the graph are neuronal specific interacting partners not detected in a control bio-GFP-KIF1A(657-1105) AP-MS experiment performed in HEK293 cells. See also Table S1.

(B) Gene ontology analysis (cellular component) of KIF1A(657-1105) interacting proteins (P-value>0.98). See also Figure S1A and Table S1.

(C) bioGFP-KIF1A(657-1105) was expressed in HEK293 cells, purified using streptavidin-pulldowns and incubated with protein extracts of cells expressing FLAG-TANC2 alone, or in combination with extracts of cells expressing HA-liprin-α2 or in combination with 10 or 40 μg of purified calmodulin (Sigma). Western blot detection was performed using FLAG, HA and GFP antibodies.

(D) bioGFP-KIF1A(657-1105) was expressed in HEK293 cells, purified and incubated with protein extracts of cells expressing HA-liprin-α2 alone, or in combination with extracts of cells expressing FLAG-TANC2 or in combination with 10 or 40 ug of purified calmodulin (Sigma). Western blot detection was performed using HA, FLAG and GFP antibodies.

(E) bioGFP-KIF1A(657-1105) was expressed in HEK293 cells, purified using streptavidin-pulldowns and incubated with protein extracts of cells expressing HA-CaM alone, or in combination with extracts of cells expressing FLAG-TANC2 or in combination with extracts of cells expressing HA-liprin-α2. Western blot detection was performed using HA, FLAG and GFP antibodies.

(F) Western blots of HA-KIF1A(657-1105) in AP experiments of full length GFP-TANC2 and GFP-TANC2 fragments (1-832, 833-1227, 1228-1500, 1501-1900) from co-transfected HEK293 cells.

(G) Western blots of HA-liprin-α2 in AP experiments of GFP, full length GFP-TANC2, or GFP-TANC2 fragments (1-832, 833-1227, 1228-1500, 1501-1900).

(H) Western blots of HA-TANC2 in AP experiments of GFP, full length GFP-liprin-α2, GFP-liprin-α2(1−735) or GFP-liprin-α2(796−1257).
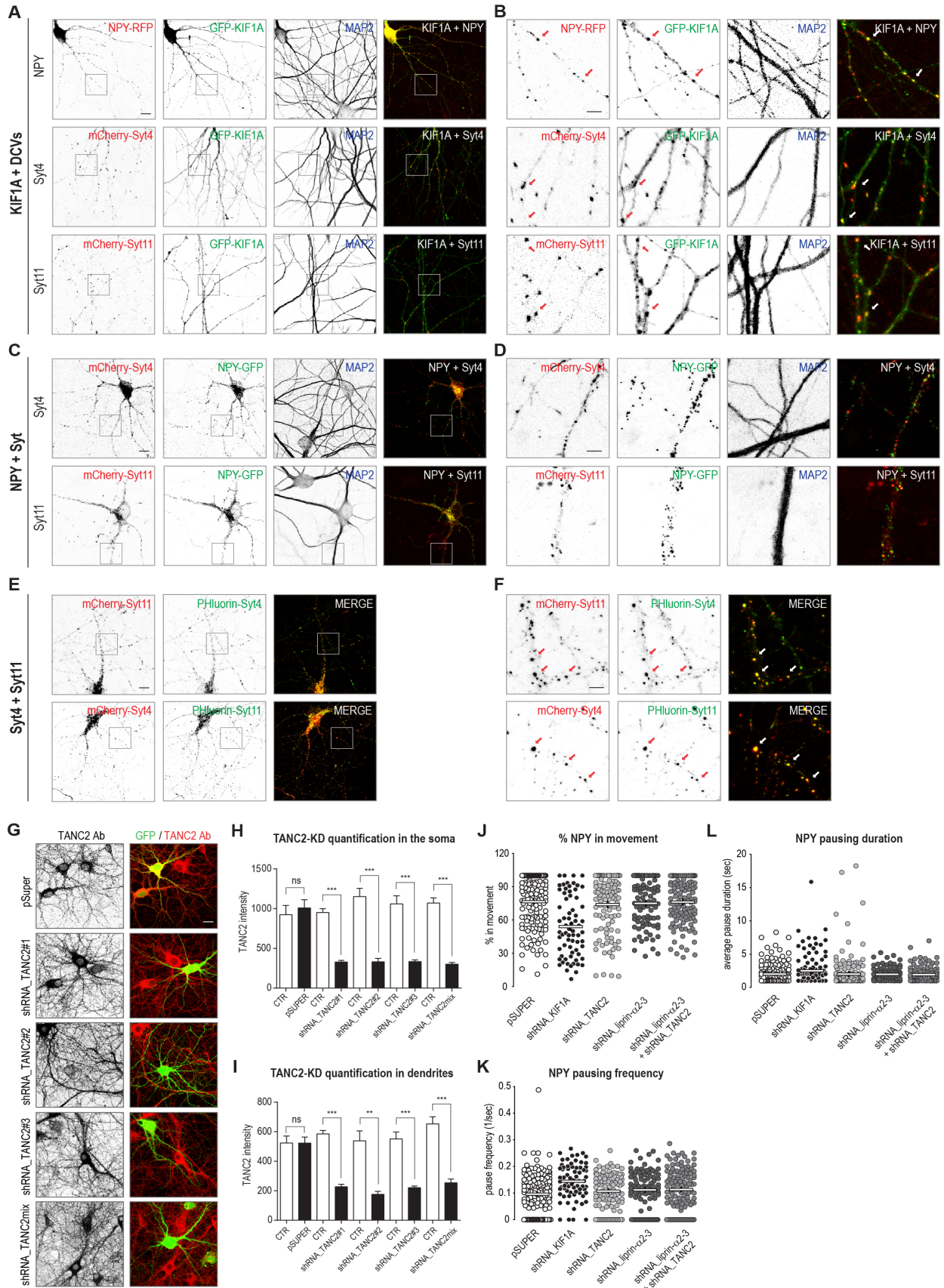
Figure S2
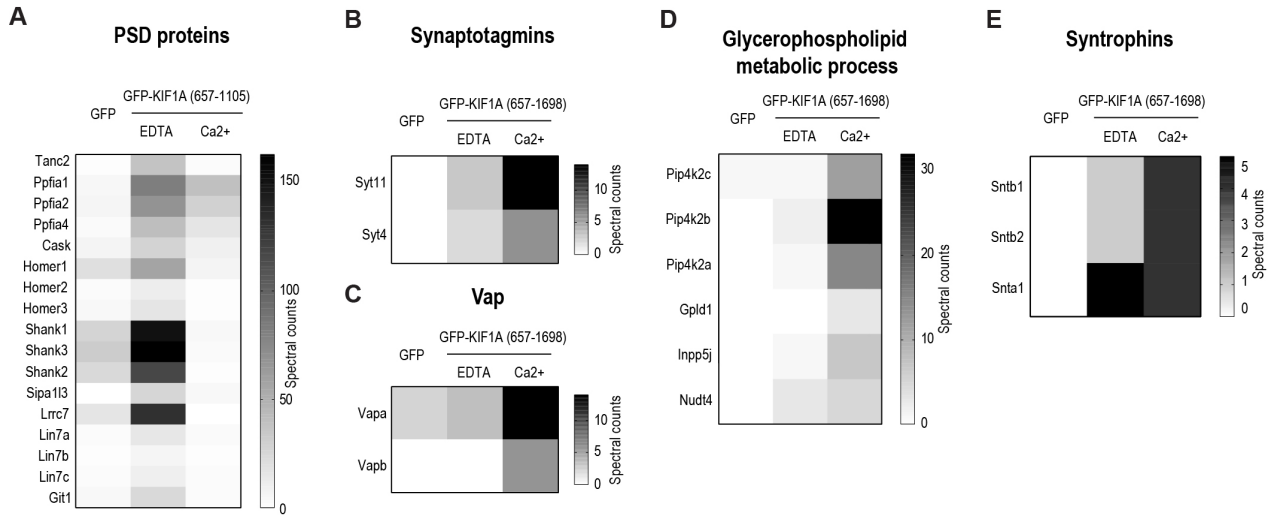
Figure S2. Related to Figure 3. KIF1A interactome is modulated by calcium

(A) BioGFP-KIF1A(657-1105) was incubated with rat brain extracts in presence of 2mM EDTA or 2mM Ca^{2+}. Heat map shows selected post synaptic density (PSD) proteins co-purified with KIF1A(657-1105)_EDTA and identified by MS. Relative abundance of each protein is represented as total spectral counts detected in bioGFP (ctr), bioGFP-KIF1A(657-1105)_EDTA or bioGFP-KIF1A(657-1105)_Ca^{2+}.

(B-E) BioGFP-KIF1A(657-1698) was incubated with rat brain extracts in presence of 2mM EDTA or 2mM Ca^{2+}. Relative abundance of each protein is represented as total spectral counts detected in bioGFP (ctr), bioGFP-KIF1A(657-1698)_EDTA or bioGFP-KIF1A(657-1698)_Ca^{2+}. Heat maps show selected co-purified proteins with KIF1A(657-1698)_Ca^{2+}: Synaptotagmin4 (Syt4) and synaptotagmin11 (Syt11) (B); Vapa and Vapb(C); phosphatidylinositol 5-phosphate 4-kinase (Pip4k2), phosphatidylinositol-glycan-specific phospholipase D (Gpld1), inositol polyphosphate 5-phosphatase (Inpp5), diphosphoinositol polyphosphate phosphohydrolase 2 (Nudt4) (D); syntrophins (Snt) (E).

Figure S3

Figure S3. Related to Figure 5. KIF1A transports DCVs in dendrites but DCV motility is not influenced by TANC2 and liprin-α

(A) Representative images of rat hippocampal neurons (DIV11-DIV14) co-transfected with GFP-KIF1A (green) in combination with NPY-RFP (red), mCherry-Syt4 (red) or mCherry-Syt11 (red) and stained for MAP2 (blue). Scale bar, 10μm.

(B) Images correspond to higher magnifications of the selected areas highlighted in the nearby figures. Arrows point to co-localizing puncta. Scale bar, 5μm.

(C) Neurons co-transfected with NPY-GFP (green) in combination with mCherry-Syt4 (red) or mCherry-Syt11 (red) and stained for MAP2 (blue). Scale bar, 10μm.

(D) Images correspond to higher magnifications of the selected areas highlighted in the nearby figures. Scale bar, 5μm.

(E) Neurons co-transfected with Phluorin-Syt4 (green) in combination with mCherry-Syt11 (red), or with Phluorin-Syt11 (green) in combination with mCherry-Syt4 (red). Scale bar, 10μm.

(F) Images correspond to higher magnifications of the selected areas highlighted in the nearby figures. Arrows point to co-localizing puncta. Scale bar, 5μm.

(G) Representative images of hippocampal neurons (DIV11-14) knockdown for TANC2 with indicated shRNA constructs (shRNA_TANC2#1, shRNA_TANC2#2, shRNA_TANC2#3, shRNA_TANC2mix), filled with GFP (green) and stained with TANC2 polyclonal antibody (red). Scale bar, 20μm.

(H-I) Quantifications of TANC2 fluorescent-staining intensities in KD-neurons shown in Figure S3G. (H) TANC2 staining intensity in the soma of transfected KD-neurons is compared to TANC2 intensity in the soma of non-transfected neurons within the same images; (I) TANC2 staining intensity in neurites of transfected KD-neurons is compared to TANC2 intensity in neurites of non-transfected neurons within the same images. The bars show mean ± s.e.m. (n=9-13 neurons (H), n=27-39 neurites (I); $^{**}P<0.01$, *paired t*-test; $^{***}P<0.001$, *paired t*-test).

(J-L) Quantifications of NPY trafficking parameters in dendrites of neurons (DIV11-14) co-transfected with NPY-GFP in combination with pSuper, shRNA_KIF1A, shRNA_TANC2, shRNA_liprin-α2−3, sh_RNA_liprin-2-3 + sh_RNA_TANC2; percentage of NPY vesicles in movement (J), NPY pause frequency (K), NPY average pause duration (L). Bars show the mean; (n=17-58 dendrites).
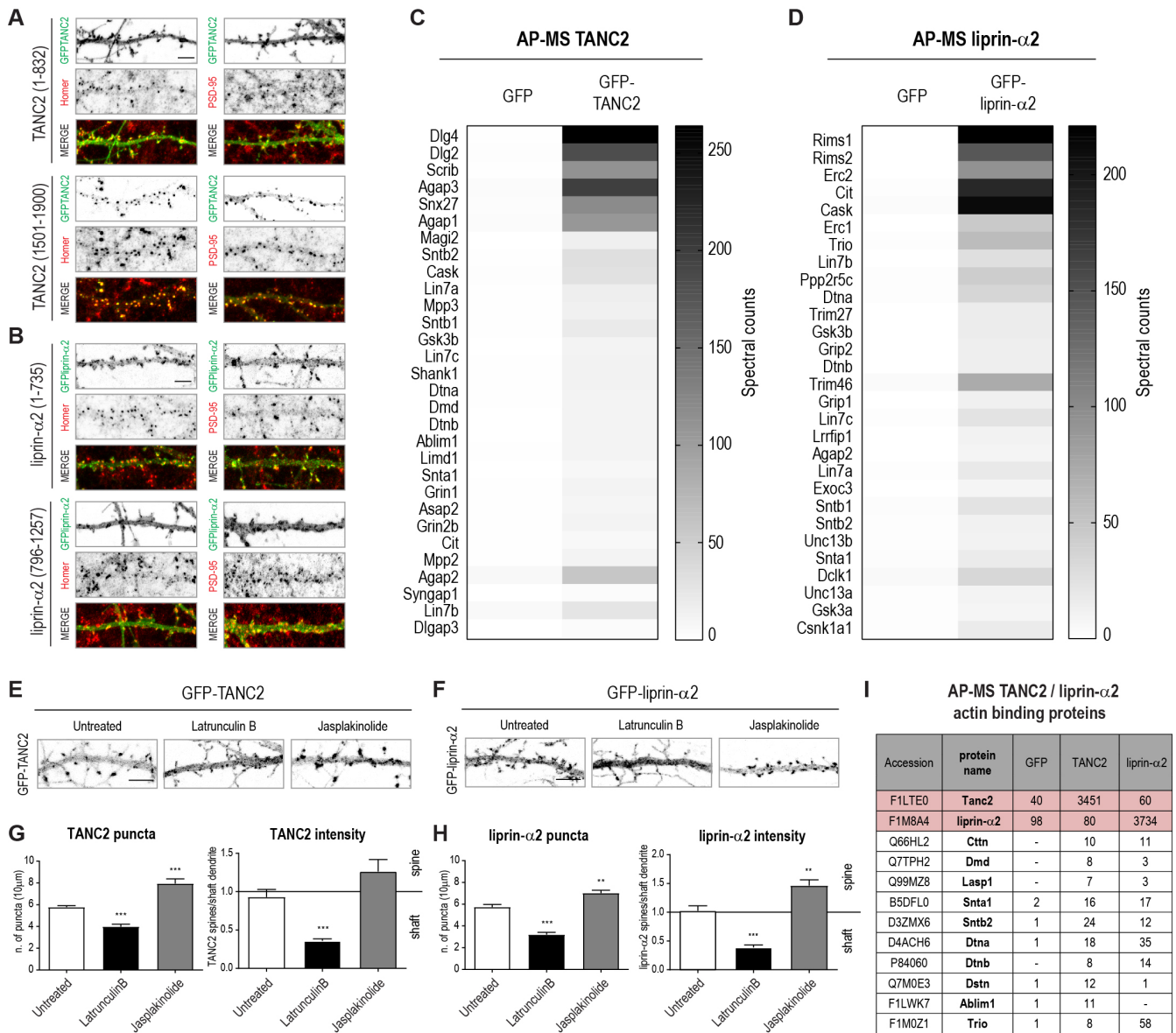
Figure S4. Related to Figure 6. TANC2 and liprin-α2 are scaffolding proteins in the post synaptic density (PSD)

(A) Representative dendritic protrusions of neurons (DIV14-17) expressing GFP-TANC2 n-terminal (1-832) or GFP-TANC2 c-terminal fragment (1501-1900) and stained for the post-synaptic proteins Homer or PSD-95 (red). Scale bar, 5μm.

(B) Representative dendritic protrusions of neurons (DIV14-17) expressing GFP-liprin-α2 n-terminal (1-735) or GFP-liprin-α2 c-terminal fragment (796-1257) and stained for the post-synaptic proteins Homer or PSD-95 (red). Scale bar, 5μm.

(C) List of significant TANC2 interactors identified by MS in AP experiments using bioGFP-TANC2 as bait. BioGFP-CTR and bioGFP-TANC2 were expressed in HEK293 cells, purified using streptavidin-pulldowns and then incubated with rat brain extracts. Co-purified proteins have been identified by AP-MS and have been classified as TANC2 interactors if

probability >0.90 using the SAINT algorithm. Heat map shows total spectral counts in bioGFP-CTR and bioGFP-TANC2. See also Table S3.

(D) List of significant liprin-α2 interactors identified by LC/MS-MS in AP experiments using bioGFP-liprin-α2 as bait. BioGFP-CTR and bioGFP-liprin-α2 were purified using streptavidin-pulldowns and then incubated with rat brain extracts. Co-purified proteins have been identified by AP-MS and have been classified as putative liprin-α2 interactors if probability >0.90 using the SAINT algorithm. Heat map shows total spectral counts in bioGFP-CTR and bioGFP-liprin-α2. See also Table S4.

(E) Dendritic protrusions of neurons (DIV14-17) expressing GFP-TANC2 and treated with DMSO (Untreated), LatrunculinB or Jasplakinolide for 1h. Scale bar, 5μm.

(F) Dendritic protrusions of neurons (DIV14-17) expressing GFP-liprin-α2 and treated with DMSO (Untreated), LatrunculinB or Jasplakinolide for 1h. Scale bar, 5μm.

(G) Quantifications of total GFP-TANC2 puncta in dendrites (left panel) and of TANC2 intensity in spines/dendritic shaft (right panel) in DMSO (Untreated), Latrunculin B or Jasplakinolide treated neurons (Figure S4E). The bars show mean ± s.e.m. (n=27-30 dendrites; ***P<0.001, t-test).

(H) Quantifications of total GFP-liprin-α2 puncta in dendrites (left panel) and of liprin-α2 intensity in spines/dendritic shaft (right panel) in DMSO (Untreated), Latrunculin B or Jasplakinolide treated neurons (Figure S4F). The bars show mean ± s.e.m. (n=24-31 dendrites, **P<0.01, t-test, ***P<0.001, t-test).

(I) Table represents selected actin binding proteins co-purified with bioGFP-TANC2 or bioGFP-liprin-α2 and identified by MS (Cttn=Cortactin, Dmd=Dystrophin, Lasp1=LIM and SH3 domain protein 1, Snt=Syntrophin, Dtn=Dystrobrevin, Dstn=Destrin, Ablim=Actin-binding LIM protein, Trio=Triple functional domain protein). Relative abundance of each protein is represented as total spectral counts. See also Table S3-4.

Figure S5
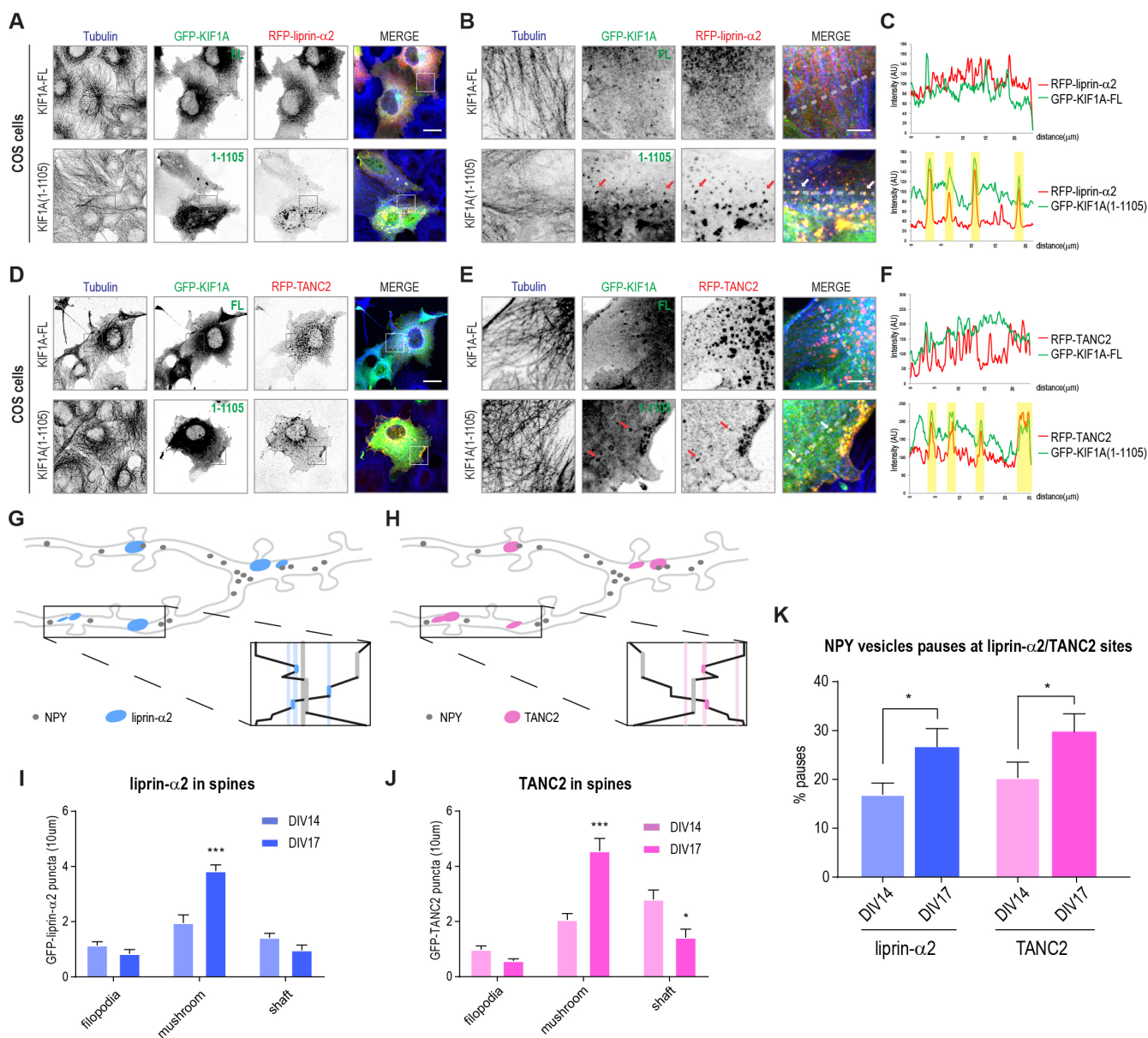
Figure S5. Related to Figure 7. TANC2 and liprin-α2 act as synaptic signposts tethering KIF1A-transported DCVs

(A) Representative images of COS7 cells co-transfected with GFP-KIF1A_full length or GFP-KIF1A(1-1105) (green) in combination with RFP-liprin-α2 (red) and stained for α-tubulin (blue). Scale bar, 20μm.

(B) Images correspond to higher magnifications of the selected areas highlighted in the nearby figures. Arrows point to co-localizing puncta. Scale bar, 5μm.

(C) Line scans of fluorescence intensity of GFP-KIF1A and RFP-liprin-α2 in Figure S5B along the transparent white line.

(D) Representative images of COS7 cells co-transfected with GFP-KIF1A_full length or GFP-KIF1A(1-1105) (green) in combination with RFP-TANC2 (red) and stained for α-tubulin (blue). Scale bar, 20μm.

(E) Images correspond to higher magnifications of the selected areas highlighted in the nearby figures. Arrows point to co-localizing puncta. Scale bar, 5μm.

(F) Line scans of fluorescence intensity of GFP-KIF1A and RFP-TANC2 in Figure S5E along the transparent white line.

(G-H) Graphical representation of NPY vesicles pausing at liprin-α2 (G) or TANC2 (H) static synaptic clusters.

(I-J) Quantifications of GFP-liprin-α2 (I) or GFP-TANC2 (J) puncta in filopodia, mushroom spines or dendritic shaft in DIV14/DIV17 neurons. The bars show mean ± s.e.m. (n=31-63 dendrites; $^*P<0.05$, t-test, $^{***}P<0.001$, t-test).

(K) Quantifications of percentage of NPY vesicles pauses at liprin-α2/TANC2 immobile clusters calculated on the total amount of NPY vesicles pauses, in DIV14/DIV17 neurons. The bars show mean ± s.e.m. (n=15-31 dendrites, $^*P<0.05$, t-test).

Figure S6
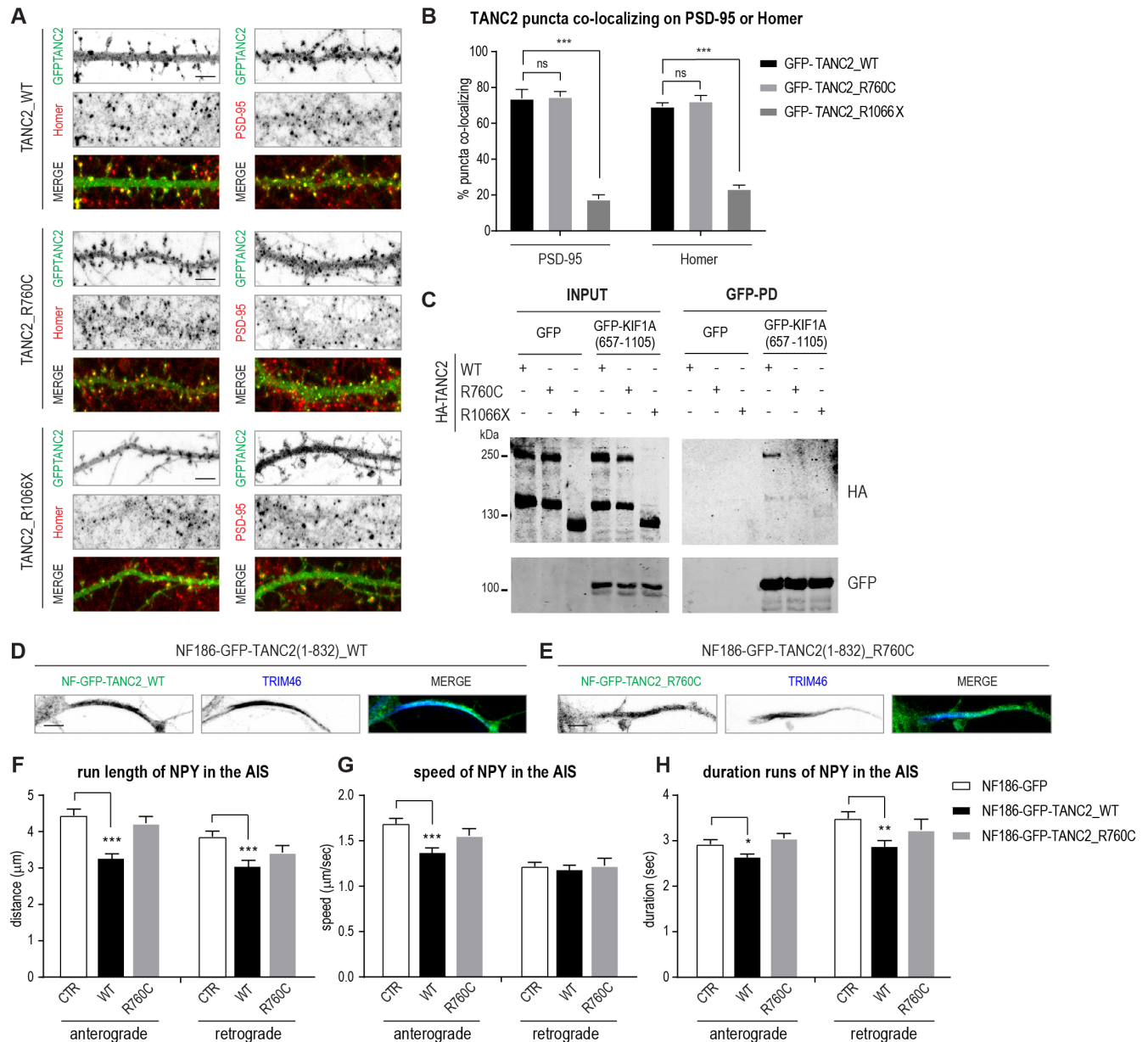
Figure S6. Related to Figure 7. TANC2 disease mutations affect KIF1A binding and DCV recruitment

(A) Representative dendritic protrusions of neurons (DIV14-17) expressing GFP-TANC2_WT, GFP-TANC2_R760C or GFP-TANC2_R1066X (green) and stained for the post-synaptic markers Homer or PSD-95 (red). Scale bar, 5μm.

(B) Quantifications corresponding to the percentage of GFP-TANC2 co-localizing puncta with endogenous Homer or PSD-95 shown in Figure S6A. The bars show mean ± s.e.m. (n=20-33 dendrites, ***P<0.001, t-test).

(C) Western blots of HA-TANC2_WT, HA-TANC_R760C and HA-TANC2_R1066X in AP experiments of bioGFP or bioGFP-KIF1A(657-1105) from co-transfected HEK293 cells.

(D-E) Zoom of the proximal axon in DIV11 hippocampal neurons transfected with NF186-GFP-TANC2(1-832)_WT (WT) (D) or NF186-GFP-TANC2(1-832)_R760C (R760C) (E) and stained for TRIM46 (blue). Scale bar, 5μm.

(F-H) Quantifications of average run length (F), speed (G) and run duration (H) of anterograde/retrograde transport of NPY-RFP vesicles in the AIS of neurons co-expressing NF186-GFP (CTR), NF186-GFP-TANC2(1-832)_WT (WT) or NF186-GFP-TANC2(1-832)_R760C (R760C). The bars show mean ± s.e.m. (n=37-40 neurons; n=202-412 vesicles; *P<0.05, t-test, **P<0.01, t-test, ***P<0.001, t-test).

SUPPLEMENTAL EXPERIMENTAL PROCEDURES

Animals

All experiments were approved by the DEC Dutch Animal Experiments Committee (Dier Experimenten Commisie), performed in line with institutional guidelines of Utrecht University and conducted in agreement with the Dutch law (Wet op de Dierproven, 1996) and European regulations (Directive 2010/63/EU). Female pregnant Wister rats were obtained from Janvier Laboratories. Upon delivery, rats were kept in a controlled 12h light-dark cycle with a temperature of 22°C and were given unrestricted access to food and water. The animals were housed with companions in transparent Plexiglas cages with wood-chip bedding and paper tissue for nest building and cage enrichment. Hippocampal neurons were obtained from embryos of both genders at E18 stage of development. None of the parameters analyzed in this study are reported to be affected by embryo gender. Pregnant female rats and embryos have not been involved in previous procedures.

Antibodies and reagents

The following primary and secondary antibodies were used in this study: Homer rabbit (SySy), PSD-95 mouse (NeuroMab), TRIM46 rabbit (van Beuningen et al., 2015),Tubα1a rabbit (Abcam), GFP rabbit (Abcam), MAP2 mouse (Sigma), MAP2 rabbit (Cell Signaling), mCherry mouse (Clontech), HA mouse (Covance), HA rabbit (Santa Cruz), FLAG mouse (Sigma), TANC1 rabbit (Abcam), TANC2 rabbit (Abcam), PanTANC (Han et al., 2010), and liprin-α1 (Spangler et al., 2013). Alexa405-, Alexa 488-, Alexa 568- and Alexa 594-conjugated secondary antibodies (Invitrogen). Other reagents used in this study include: jasplakinolide (2792, Tocris Bioscience), latrunculinB (SC-203318, Bioconnect), BAPTA-AM (SC-202488, Santa Cruz), bicuculline (Sigma), Streptavidin Dynabeads M-280 (Thermo Scientific), GFP-Trap® beads (ChromoTek), Calmodulin-Sepharose beads (Biovision), recombinant Calmodulin (C4874, Sigma).

Expression vectors and shRNA constructs

The following mammalian expression plasmids have been previously described: BirA coding vector and pebioGFP (van der Vaart et al., 2013), pGW1-GFP (Jaworski et al., 2009), pSuper vector (Brummelkamp et al., 2002), pGW2-MARCKS-GFP (Schatzle et al., 2011), pGW1-HA-liprin-α2, pGW1-GFP-liprin-α2, pGW1-GFP-liprin-α2(1-735), pGW1-GFP-liprin-α2(796-1257) and peBioGFP-liprin-α2 (Spangler et al., 2013), pGW1-HA-KIF1A (Kevenaar et al., 2016), pGW1-GFP-KIF1A (Lee et al., 2003), pGW2-NPY-GFP and pGW2-NPY-RFP (Schlager et al., 2010). pGW2-MARCKS-BFP was cloned by replacing GFP with cDNA encoding for BFP using BamHI and XbaI sites. pAAV-mCherry-Syt4, pAAV-mCherry-Syt11, pAAV-Syt4-phluorin, pAAV-Syt11-phluorin were kindly given us by Camin Dean. HA-CaM was generated by PCR on human-CAM1 cDNA kindly given us by Mike Boxem and cloned into a pGW2-HA linearized backbone using AscI and BamHI.

PebioGFP-KIF1A(657-1105), pebioGFP-KIF1A(393-881), pebioGFP-KIF1A(1105-1698), pebioGFP-KIF1A(950-1250), pebioGFP-KIF1A(657-1698) correspond to truncated versions of the KIF1A rat variant 2 (XM_003750741) and were kindly given us by Gary Banker; pebioGFP-KIF1A(691-752), (830-896), (986-1054) were produced by PCRs using pebioGFP-KIF1A(657-1105) as template and cloned using BamHI and XbaI sites; pebioGFP-KIF1A(657-1105)_5*Ala mutant was generated by gibson cloning (New England Biolabs) using 3 fragments: 1) gene blocks (IDT) to introduce 5 point mutations within the predicted CaM binding site (W714A, W716A, Y717A, F719A and L722A) (360b), 2) PCR product of pebioGFP-KIF1A657-1105 and 3) peBioGFP backbone digested with BamHI and AscI; pebioGFP-KIF1A657-1698_5*Ala mutant was generated with the same strategy but using the pebioGFP-KIF1A657-1698 as substrate for PCR of fragment 2; pGW1-HA-KIF1A(657-1105), pGW1-HA-KIF1A(657-1105)_5*Ala, pGW1-HA-KIF1A(657-1698), pGW1-HA-KIF1A(657-1698)_5*Ala were created using PCR based strategies and cloned into pGW1-HA vector using AscI and EcoRI sites; pGW1-GFP-KIF1A_5*Ala was created by Gibson cloning using 3 fragments: 1) pGW1-GFP-KIF1A digested with KpnI and BamHI 2-3) PCR products obtained using degenerated primers to introduce 5 point mutations in the CaM binding site; pGW1-HA-KIF1A(1-1105) was generated by PCR on pGW1-HA-KIF1A and cloned using AscI and EcoRI.

pGW2-HA-TANC1 and pGW2-HA-TANC2 were generated using FLAG-TANC1 and FLAG-TANC2 (Han et al., 2010) as templates respectively and gene blocks (IDT) for the N-terminal part of the proteins and cloned into a pGW2-HA backbone using AscI and BamHI sites; peBioGFP-TANC2, b-actin-GFP-TANC2, b-actin-myc-tagRFP-TANC2 were generated using as template pGW2-HA-TANC2; b-actin-GFP-TANC2(1-832, 833-1227, 1228-1500, 1501-1900) were created by PCR strategies and cloned into b-actin-GFP vector using AscI and BamHI sites; pGW2-HA-TANC2_R760C and pGW2-HA-TANC2_R1066X were generated by Gibson cloning using pGW2-HA-TANC2_WT as template for PCRs and a pGW2-HA linearized backbone; b-actin-GFP-TANC2_R760C and b-actin-GFP-TANC2_ R1066X were generated by PCR based strategies using b-actin-GFP-TANC2 as backbone and pGW2-HA-TANC2_R760C and pGW2-HA-TANC2_R1066X as templates for PCR reactions. pGW1-NF186-GFP-TANC2(1-832)_WT and _R760C were produced by PCRs based strategies using b-actin-GFP-TANC2_WT or _R760C as templates and by cloning these PCRs products into a pGW1-NF186 (Kuijpers et al., 2016) backbone using AscI/XbaI sites.

The following shRNA sequences are used in this study: TANC2#1 (5'-CCTCAGTCAAGGGTCATAT), TANC2#2 (5'-GGAGCTGAAACCGAAATCT) and TANC2#3 (5'-GGCCAGTAAATACCAATCT) targeting rat TANC2 mRNA (XM_008768351.1) were designed using the siRNA selection program at the Whitehead Institute for Biomedical Research (jura.wi.mit.edu/bioc/siRNAext) (Yuan et al., 2004) and the complementary oligonucleotides were annealed and inserted

into a pSuper vector (Brummelkamp et al., 2002; Hoogenraad et al., 2005). ShRNA_KIF1A has been already described (Kevenaar et al., 2016) as well as shRNA_liprin-α2, shRNA_liprin-α3 (Spangler et al., 2013) and shRNA_cortactin (Jaworski et al., 2009). The control pSuper vector contains a scrambled sequence.

Primary hippocampal neuron cultures, transfections and drug treatments

Primary hippocampal cultures were prepared from embryonic day 18 rat brains. Cells were plated on coverslips coated with poly-L-lysine (30μg /ml) and laminin (2μg/ml) at a density of 100.000/well as previously described (Goslin and Banker, 1989; Kapitein et al., 2010). Hippocampal cultures were grown in Neurobasal medium (NB) supplemented with B27, 0.5 mM glutamine, 12.5 μM glutamate and penicillin/streptomycin.

Hippocampal neurons at DIV 11-14 / 14-17 were transfected using Lipofectamine 2000 (Invitrogen). Briefly, DNA (1.8 μg/well, for a 12 wells plate) was mixed with 3.3 μl of Lipofectamine 2000 in 200 μl NB, incubated for 30 min, and then added to the neurons in NB at 37°C in 5% CO2 for 45 min. Next, neurons were washed with NB and transferred in their original medium at 37°C in 5% CO2 for 2-3 days. 10 μM latrunculin B, 10 μM jasplakinolide, 10 μM BAPTA-AM or 40μM bicuculline were added to neuron cultures and fixed or imaged from 0 to 1h after addition.

Affinity Purification-Western blot (AP-WB) using biotin or GFP pull-down

Human Embryonic Kidney 293 cells (HEK293) cells were cultured in DMEM/Ham's F10 (50%/50%) containing 10% Fetal Calf Serum (FCS) and 1% penicillin/streptomycin at 37°C and 5% CO2. HEK293 cells were transfected with pe-Biotin-GFP constructs in combination with BirA or with GFP tagged constructs using polyethylenimine (PEI, Polysciences) according to the manufacturer instructions. Cells were lysed 48h later in lysis buffer (50mM TrisHCl (PH 7.4-7.8), 100mM NaCl, 0.5% TX-100, 5mM MgCl2, protease inhibitors (Roche)), centrifuged at 13.000 rpm for 15 min and the supernatants were incubated with either Streptavidin Dynabeads M-280 (Thermo Scientific) or GFP-trap beads (Chromotek) for 1h at 4°C. Beads were then separated using a magnet (Dynal, Invitrogen) and washed five times in washing buffer (20mM Tris HCl, 150mM KCl, 0.1% TritonX-100). Proteins were eluted from the beads by adding a 4x dilution of the sample buffer (8% SDS, 25% glycerol, 0.05M Tris pH 6.8, 400mM DTT and 40mg/l bromophenol blue). Samples were then boiled at 99ºC for 10 minutes before being analyzed by SDS PAGE. Proteins were transferred on nitrocellulose membranes (Millipore) using a semi-dry blotting system. Membranes were blocked with 3% BSA in PBS-T (0.1% Tween-20) and incubated with primary antibodies (overnight at 4°C) in 3% BSA PBS-T. IRdye680 or IRdye800-conjugated secondary antibodies (Li-Cor) were diluted 1:20.000 in 3%BSA-PBST and applied for 1h at RT. Blots were acquired using a LICOR Odyssey scanner at 680nm or 800nm. To quantify the relative amount of a specific co-precipitated protein, the intensity of each band was measured and then normalized to the intensities of the corresponding INPUT loading control band and to the intensity of the band relative to the purified bait protein. Quantifications were performed with Image J software (Universal Imaging Corporation).

Affinity Purification-Mass spectrometry (AP-MS) using biotin or GFP pull-down on rat brain extracts

Human Embryonic Kidney 293 cells (HEK293) cells were cultured in DMEM/Ham's F10 (50%/50%) containing 10% Fetal Calf Serum (FCS) and 1% penicillin/streptomycin at 37°C and 5% CO2. HEK293 cells were transfected with pe-Biotin-GFP constructs in combination with BirA or with GFP-constructs using polyethylenimine (PEI, Polysciences) according to

the manufacturer instructions. Cells were lysed 48h later in RIPA lysis buffer (50mM TrisHCl pH 7.4-7.8, 150mM NaCl, 1%Triton X-100, 0.1% SDS, 0.5% Sodium Deoxycholate and Protease inhibitors (Roche)), centrifuged at 13.000 rpm for 15 min and the supernatants were incubated for 1h at 4°C with either Streptavidin Dynabeads M-280 (Thermo Scientific) or GFP-trap beads (Chromotek), previously blocked in chicken egg albumin (Life Technologies). Beads were then separated using a magnet (Dynal, Invitrogen) washed twice in low salt washing buffer (20mM Tris-HCl pH 7.4-7.8, 100 mM KCl, 0.1% Triton X-100), followed by two washing steps in high salt wash buffer (20mM Tris-HCl pH 7.4-7.8, 500 mM KCl, 0.1% Triton X-100) and two final steps in low salt washing buffer (20mM Tris-HCl pH 7.4-7.8, 100 mM KCl, 0.1% Triton X-100) to remove binding proteins from HEK293 cells. Brains were obtained from female adult rats and homogenized in 10x volume/weight in tissue lysis buffer (50mM TrisHCl, 150mM NaCl, 0.1% SDS, 0.2% NP-40, and protease inhibitors). Brain lysates were centrifuged at 16,000 g for 15 min at 4°C and the supernatant was then incubated for 1h at 4°C with beads previously conjugated with either the biotinylated or the GFP-tagged proteins of interest. Beads were then separated using a magnet (Dynal; Invitrogen) and washed in normal washing buffer (20mM Tris HCl, 150mM KCl, 0.1% TritonX-100) for five times. For MS analysis, the beads were resuspended in 15 μl of Laemmli Sample buffer (Biorad), boiled at 99ºC for 10 minutes and supernatants were loaded on 4-12% Criterion XT Bis-Tris precast gel (Biorad). The gel was fixed with 40% methanol and 10% acetic acid and then stained for 1h using colloidal coomassie dye G-250 (Gel Code Blue Stain Reagent, Thermo Scientific). Each lane from the gel was cut in 3 slices, destained and digested using trypsin, as described in (Ekkebus et al., 2013). Briefly, each lane from the gel was cut into three pieces and placed in 0.5-ml tubes. Gel pieces were then washed with 250 μl of water, followed by 15 min dehydration in acetonitrile. Proteins were reduced (10 mM dithiothreitol, 1h at 56°C), dehydrated and alkylated (55 mM iodoacetamide, 1h in the dark). After two rounds of dehydration, trypsin (Promega) was added to the samples (20 μl of 0.1 mg/ml trypsin in 50 mM Ammoniumbicarbonate) and incubated overnight at 37°C. Peptides were extracted with ACN, dried down and reconstituted in 10% formic acid prior MS analysis.

In vitro Co-purification of KIF1A using sepharose CaM beads
Equal amounts of lysates from HEK293 cells transfected with KIF1A(657-1105) or KIF1A(657-1105)5*Ala were incubated for 4h at 4°C with Calmodulin-Sepharose beads (Biovision) with increasing μM concentration of Ca^{2+} or EDTA. Beads were then washed with normal washing buffer (20mM Tris HCl, 150mM KCl, 0.1% TritonX-100) for 3 times by centrifuging them at 1500g for 3min. Proteins were eluted from the beads by adding a 4x dilution of the sample buffer (8% SDS, 25% glycerol, 0.05M Tris pH 6.8, 400mM DTT and 40mg/l bromophenol blue). Samples were then boiled at 99ºC for 10 minutes before being analyzed by SDS PAGE.

Immunoprecipitation on rat brain extracts
Rat brain extracts were obtained from female adult rats and homogenized in 10x volume/weight in tissue lysis buffer (50mM TrisHCl, 150mM NaCl, 0.1% SDS, 0.2% NP-40, and protease inhibitors). Brain lysates were centrifuged at 16.000 g for 15 min at 4°C and the supernatant was used for the immunoprecipitations. IPs were performed using Pierce Crosslink IP kit (Thermo Scientific) according to manufacturer recommended protocol. TANC1 rabbit (Abcam), TANC2 rabbit (Abcam), PanTANC (Han et al., 2010) were the antibodies used for the IP experiments.

Mass spectrometry analysis

All samples were analyzed on an ETD enabled LTQ-Orbitrap Elite coupled to Proxeon EASY-nLC 1000 (Thermo Fisher Scientific, Odense, Denmark) or on an Orbitrap Q-Exactive mass spectrometer (Thermo Fisher Scientific, Bremen, Germany) coupled to an Agilent 1290 Infinity LC (Agilent Technologies). Peptides were loaded onto a trap column (Reprosil pur C18, Dr. Maisch, 100 µm x 2 cm, 3 µm; constructed in-house) with solvent A (0.1% formic acid in water) at a maximum pressure of 800 bar and chromatographically separated over the analytical column (Poroshell 120 EC C18, Agilent Technologies, 50 µm x 50 cm, 2.7 µm) using 90 min linear gradient from 7-30% solvent B (0.1% formic acid in acetonitrile) at a flow rate of 150 nL/min. The mass spectrometers were used in a data-dependent mode, which automatically switched between MS and MS/MS. After a survey scan from 350-1500 m/z the 10 or 20 most abundant peptides were subjected to either CID or HCD fragmentation depending on the MS-spectrometer used. MS spectra were acquired in high-resolution mode (R > 30,000), whereas MS2 was in high-sensitivity mode (R > 15,000). For data analysis, raw files were processed using Proteome Discoverer 1.4 (version 1.4.1.14, Thermo Scientific, Bremen, Germany). Database search was performed using the Uniprot rat database and Mascot (version 2.5.1, Matrix Science, UK) as the search engine. Carbamidomethylation of cysteines was set as a fixed modification and oxidation of methionine was set as a variable modification. Trypsin was set as cleavage specificity, allowing a maximum of 2 missed cleavages. Data filtering was performed using a percolator (Kall et al., 2007), resulting in 1% false discovery rate (FDR). Additional filters were search engine rank 1 and mascot ion score >20. The mass spectrometry proteomics data have been deposited to the ProteomeXchange Consortium via the PRIDE (Vizcaino et al., 2016) partner repository with the dataset identifier PXD010080.

Cross linking Mass Spectrometry (XL-MS)

For crosslinking experiment, the beads with affinity-precipitated proteins were incubated with 2 mM disuccinimidyl sulfoxide (DSSO; ThermoFischer Scientific) crosslinker for 1h at room temperature (Kao et al., 2011). The crosslinking reaction was quenched with 20 mM Tris-HCl for 20 min at room temperature. On-beads crosslinked proteins were denatured with 2 mM Urea, reduced with 4 mM dithiothreithol at 56^0C for 30 min and then alkylated with 8mM iodoacetamide for 30 min in the dark. Proteins were partially digested using trypsin (Promega) at 37^0C for 2h. The supernatant was removed from the beads, fresh aliquot of trypsin was added and further digested overnight at 37^0C. Crosslinked protein digests were subsequently desalted and enriched with Strong Cation Exchange (SCX) Stage Tips. Obtained fractions were dried and stored at -80^0C for further use.

Crosslinked peptide mixtures were reconstituted in DMSO/FA/HOH 5%/10%/85% (v/v/v) mixture and analyzed on an Orbitrap Fusion Lumos (ThermoFisher Scientific) coupled online to an Agilent UPLC 1290 system (Agilent Technologies). Crosslinked peptide digest was trapped on a pre-column (Reprosil pur C18, Dr. Maisch, 100 µm x 2 cm, 3 µm; constructed in-house) for 10 min with buffer A (0.1% formic acid) and separated on an analytical column (Poroshell 120 EC C18, Agilent Technologies, 50 µm x 50 cm, 2.7 µm) over 65 min with a linear gradient from 10% to 40% B (B: 0.1% formic acid, 80% acetonitrile). MS data acquisition was performed using MS2_MS3 acquisition strategy: at the MS^1 level survey scan was recorded in Orbitrap (OT) at 60.000 resolution. For selected precursors collisional-induced dissociation (CID) was applied and signature peaks for the crosslinkers were recorded at 30000 resolution. Fragments exhibiting patterns associated to the DSSO cleavable crosslinker were further subjected to low-resolution MS^3 scan in the ion trap (IT) (Kao et al., 2011;

Liu et al., 2017). Raw data files were processed in Proteome Discoverer 2.2 with in-house developed nodes for crosslink analysis (Liu et al., 2015). The mass spectrometry proteomics data have been deposited to the ProteomeXchange Consortium via the PRIDE (Vizcaino et al., 2016) partner repository with the dataset identifier PXD010080.

Bioinformatic analysis

Gene ontology (GO) classification was obtained via PANTER (Mi et al., 2005). Statistical assessment of the AP-MS data was performed based on spectral counts using the SAINT (Significance Analysis of INTeractions, version 2.3.2) algorithm (Choi et al., 2011) . The SAINT parameters were set as follows: nburn=2000, niter=20.000, lowmode=0, minfold=0, and norm=1. Bait proteins with a SAINT probability score >0.90 were considered putative protein interaction partners.

Immunofluorescent staining

Neurons were fixed for 10 min with 4% formaldehyde/4% sucrose in phosphate-buffered saline (PBS) at room temperature. After fixation cells were washed three times for 10 min in PBS, incubated for 10 min with permeabilization buffer (0.25% TritonX-100 in PBS) and then blocked for 1h with blocking buffer (2% BSA, 2% Glycin, 0.2% Gelatin, 50mM NH_4Cl, in PBS). Neurons were then incubated with primary antibodies diluted in blocking buffer overnight at 4°C, washed three times in PBS for 10 min and then incubated with Alexa-conjugated secondary antibodies in blocking buffer for 1h at room temperature. Neurons were then washed 3 times for 5 min in PBS at room temperature and subsequently mounted on slides in Vectashield mounting medium (Vector Laboratories). Confocal images were acquired using a LSM 700 confocal laser-scanning microscope (Zeiss) with a 40×1.3 N.A or 63×1.4 N.A. oil objective (Zeiss). Each image was a z-series of ~7-10 images, each averaged 2 times and was chosen to cover the entire region of interest from top to bottom. The resulting z-stack was ''flattened'' into a single image using maximum projection. Images were not further processed and were of similar high quality to the original single planes. The confocal settings were kept the same for all scans when fluorescence intensity was compared. Morphometric analysis, quantification, and co-localization were performed using ImageJ software (Universal Imaging Corporation). See for details the methods section: Image analysis and quantification.

Image analysis and quantification

Quantification of TANC2 knockdown efficiency by immunostaining in cultured hippocampal neurons

Efficiency of TANC2 shRNAs knock down was verified by immunostaining of endogenous TANC2 protein in hippocampal neurons co-transfected at DIV11 with 0.45 μg/well GFP and 1.35 μg/well of different TANC2-shRNAs or a mixture of all of them, and fixed 3 days later (DIV14). TANC2 staining (rabbit polyclonal anti-TANC2 antibody, Abcam) was measured both in the soma and in the neurites of GFP positive neurons and was compared to TANC2 corresponding staining in GFP negative surrounding cells within the same image. Images were acquired using a LSM 700 confocal laser-scanning microscope (Zeiss) using a plan-apo 40×1.3 N.A with the same settings and the exposure time and taking series of stacks from the bottom to the top. Maximum intensity projections were created using ZEN 2014 software (Zeiss) and later used for the analyses. ImageJ was used to manually draw specific regions of interest (ROI) located in the soma and in at least three primary neurites. From the ROIs the mean intensity was then measured. To prevent selection bias during quantification, the regions of interest in TANC2-KD neurons were selected in one channel (GFP) and blindly quantified in the other channel (TANC2 intensity). Intensities were measured in segments of approximately the same size, both in GFP positives and GFP

negatives neurons. To remove the background signal, the intensity near the selected areas (same segment size) was measured and subtracted to the measured intensities within the same image. Normalized intensities were averaged over multiple cells and a statistical analysis was performed with student's t test assuming a two-tailed and unequal variation.

Dendritic protrusions analysis

To highlight protrusions morphology, neurons were transfected at DIV11 and fixed at DIV14 using MARCKS-GFP as an unbiased cell-fill in combination with our constructs of interest up to a maximum of 1.8 μg of total DNA/well. Confocal images were acquired using a LSM700 confocal laser-scanning microscope (Zeiss) with a 63x oil objective. The confocal laser intensity settings were optimized for each neuron. The resulting z-stack used for the spine counting was a single image processed by using the maximum projection function of ZEN2014 software (Zeiss). Images were not further processed and were of similar high quality to the original single planes. Morphological analysis and quantification were performed using ImageJ. For each neuron three dendrites were selected and boxes of 20 μm of length were placed 20 μm from the soma. Within these boxes the number of mushroom, filopodia-like and stubby spines were counted manually by using the Cell Counter plugin.

Quantification of fluorescent intensity in neurons

For the quantification of fluorescent intensity, images were acquired on a LSM700 confocal microscope (Zeiss) using a plan-apo 40×1.3 N.A objective and intensity of signals in the cell body and neurites were measured using ImageJ software. Because neurites often crossed several z planes, series of stacks were taken from the bottom to the top and the ZEN 2014 software (Zeiss) was used to generate image projections for quantitative analyses. To prevent selection bias during quantification, the neurites segments were selected in one channel (GFP, RFP or BFP to visualize neuronal morphology) and quantified in the other channel. To control for background signals the intensity of an area of the same size was measured near the selected neuron and the measured random fluorescent intensity was subtracted in these images. Intensities were averaged over multiple cells and normalized.

Quantification of KIF1A and DCV distribution in dendritic spines

To highlight protrusions morphology, neurons were transfected at DIV14 and fixed at DIV17 using MARCKS-BFP as an unbiased cell-fill in combination with our constructs of interest (KIF1A, NPY, Syt4) up to a maximum of 1.8 ug of total DNA/well. Confocal images were acquired using a LSM700 confocal laser-scanning microscope (Zeiss) with a 63x oil objective. The confocal laser intensity settings were optimized for each neuron. The resulting z-stack used for the counting was a single image processed with the maximum projection function of ZEN2014 software (Zeiss). To prevent selection bias during quantification, the selected dendritic fragments were selected in the BFP channel. For each neuron three dendrites were selected and boxes of 20 μm of length were placed approximately 20 μm from the soma; then KIF1A, NPY or Syt4 puncta were counted in each single spine along 20 μm as well as in the dendritic shaft. Ratios of puncta spines/shaft were then normalized for the total number of spines along 20 μm to correct for different spines densities in different conditions.

Live cell imaging and imaging processing

Live-cell imaging experiments were performed in an inverted microscope Nikon Eclipse Ti-E (Nikon), equipped with a Plan Apo VC 100x NA 1.40 oil or a 60x NA 1.40 oil, a Yokogawa CSU-X1-A1 spinning disk confocal unit (Roper Scientific), a Photometrics Evolve 512 EMCCD camera (Roper Scientific) and an incubation chamber (Tokai Hit) mounted on a

motorized XYZ stage (Applied Scientific Instrumentation) which were all controlled using MetaMorph (Molecular Devices) software. Neurites that were in close proximity to the soma were selected for imaging.

Imaging and analysis of motility of NPY and Syt4 motility

Time-lapses were acquired with 1 sec intervals for 5min, later analyzed for motility of vesicles. Motility was analyzed by pseudocoloring 1st frame in green and 10th frame in red. Merging those frames revealed vesicles non-colocalizing (motile), partially and fully co-localizing (immotile).

Imaging and analysis of motility of KIF1A, NPY, Syt4 upon BAPTA treatment

For motility analyses, time-lapses were acquired with 1 sec intervals for 5min, later analyzed for motility of vesicles. BAPTA-AM or DMSO were pipetted to the sample at a final concentration of 10uM. Motility was analyzed by pseudocoloring 1st frame in green and 10th frame in red. Merging those frames revealed vesicles non-colocalizing (motile), partially and fully co-localizing (immotile).

Imaging and analysis of motility of KIF1A, NPY upon bicuculline treatment

Time lapse images in GFP and RFP channels were carried at 1 frame per second intervals, for 10 minutes before addition of DMSO or bicuculline. Treatments were pipetted to the sample and imaging of the same field of view was carried for another 10 minutes. To analyze the mobility of KIF1A and NPY along neurites, 3-5 neurite segments were selected from each field of view. The same segments were selected from the time lapse taken before and after addition of treatments. Only segments that were of at least 15µm in length and with minimal crossings by other neurites were selected for kymographs based analysis. Using Fiji software, segments were traced with a line-ROI and kymographs were separately created using the Multi Kymograph plugin. The number of KIF1A and co-localized, mobile KIF1A and NPY traces of each kymograph were manually counted.

Imaging and analysis of motility of KIF1A, NPY, Syt4 in combination with the scaffolding proteins liprin-α2 and TANC2.

Time-lapses were acquired with 1 sec intervals for 5min, in neurons (DIV14, DIV17) co-transfected with GFP- or RFP-tagged TANC2 or liprin-α2 in combination with GFP-, RFP- or mCherry-tagged KIF1A, NPY or Syt4. To analyze the mobility of DCVs along neurites, 3-5 neurite segments were selected from each field of view. To calculate the percentage of DCV pausing within or outside static TANC2/liprin-α2 spots, kymographs were obtained and subsequently analyzed. NPY was used as marker for DCVs. NPY pausing was calculated as percentage of the ratio of NPY pauses at TANC2/liprin-α2 positive clusters on the total amount of NPY pauses.

Imaging and analysis of NPY motility in the axon initial segment (AIS) of neurons transfected with Neurofascin-TANC2 fusion proteins.

Time lapse images in GFP and RFP channels were carried at 5 frames per second intervals, for 50 seconds. Neurons (DIV11) were co-transfected with NPY-RFP in combination with NF186-GFP or NF186-GFP-TANC2(1-832)_WT or NF186-GFP-TANC2(1-832)_R760C. The AIS of transfected neurons was clearly detectable in the green channel because of the accumulation of NF186 and NF186 chimeric proteins in this region. After the AIS was visualized in green, the RFP channel was used for the imaging of NPY vesicles in the same region. For the analysis, a z-projection of the average intensity of the movie was made and subtracted from the original movie to background fluorescence and non-moving particles. A line of approximately 10-20µm in each AIS was drawn. Kymographs of these lines were then created using KymoResliceWide plugin. Clearly visible anterograde and retrograde traces were traced on the kymos by drawing straight lines. Length and angle of the lines were measured and used to calculate velocity, run length and duration.

SUPPLEMENTAL REFERENCES

- Brummelkamp, T.R., Bernards, R., and Agami, R. (2002). Stable suppression of tumorigenicity by virus-mediated RNA interference. Cancer Cell 2, 243-247.

- Choi, H., Larsen, B., Lin, Z.Y., Breitkreutz, A., Mellacheruvu, D., Fermin, D., Qin, Z.S., Tyers, M., Gingras, A.C., and Nesvizhskii, A.I. (2011). SAINT: probabilistic scoring of affinity purification-mass spectrometry data. Nat Methods 8, 70-73.

- Ekkebus, R., van Kasteren, S.I., Kulathu, Y., Scholten, A., Berlin, I., Geurink, P.P., de Jong, A., Goerdayal, S., Neefjes, J., Heck, A.J.*, et al.* (2013). On terminal alkynes that can react with active-site cysteine nucleophiles in proteases. J Am Chem Soc 135, 2867-2870.

- Goslin, K., and Banker, G. (1989). Experimental observations on the development of polarity by hippocampal neurons in culture. J Cell Biol 108, 1507-1516.

- Han, S., Nam, J., Li, Y., Kim, S., Cho, S.H., Cho, Y.S., Choi, S.Y., Choi, J., Han, K., Kim, Y.*, et al.* (2010). Regulation of dendritic spines, spatial memory, and embryonic development by the TANC family of PSD-95-interacting proteins. J Neurosci 30, 15102-15112.

- Hoogenraad, C.C., Milstein, A.D., Ethell, I.M., Henkemeyer, M., and Sheng, M. (2005). GRIP1 controls dendrite morphogenesis by regulating EphB receptor trafficking. Nat Neurosci 8, 906-915.

- Jaworski, J., Kapitein, L.C., Gouveia, S.M., Dortland, B.R., Wulf, P.S., Grigoriev, I., Camera, P., Spangler, S.A., Di Stefano, P., Demmers, J.*, et al.* (2009). Dynamic microtubules regulate dendritic spine morphology and synaptic plasticity. Neuron 61, 85-100.

- Kall, L., Canterbury, J.D., Weston, J., Noble, W.S., and MacCoss, M.J. (2007). Semi-supervised learning for peptide identification from shotgun proteomics datasets. Nat Methods 4, 923-925.

- Kao, A., Chiu, C.L., Vellucci, D., Yang, Y., Patel, V.R., Guan, S., Randall, A., Baldi, P., Rychnovsky, S.D., and Huang, L. (2011). Development of a novel cross-linking strategy for fast and accurate identification of cross-linked peptides of protein complexes. Mol Cell Proteomics 10, M110 002212.

- Kapitein, L.C., Yau, K.W., and Hoogenraad, C.C. (2010). Microtubule dynamics in dendritic spines. Methods Cell Biol 97, 111-132.

- Kevenaar, J.T., Bianchi, S., van Spronsen, M., Olieric, N., Lipka, J., Frias, C.P., Mikhaylova, M., Harterink, M., Keijzer, N., Wulf, P.S.*, et al.* (2016). Kinesin-Binding Protein Controls Microtubule Dynamics and Cargo Trafficking by Regulating Kinesin Motor Activity. Curr Biol 26, 849-861.

- Kuijpers, M., van de Willige, D., Freal, A., Chazeau, A., Franker, M.A., Hofenk, J., Rodrigues, R.J., Kapitein, L.C., Akhmanova, A., Jaarsma, D., and Hoogenraad, C.C. (2016). Dynein Regulator NDEL1 Controls Polarized Cargo Transport at the Axon Initial Segment. Neuron 89, 461-471.

- Lee, J.R., Shin, H., Ko, J., Choi, J., Lee, H., and Kim, E. (2003). Characterization of the movement of the kinesin motor KIF1A in living cultured neurons. J Biol Chem 278, 2624-2629.

- Liu, F., Lossl, P., Scheltema, R., Viner, R., and Heck, A.J.R. (2017). Optimized fragmentation schemes and data analysis strategies for proteome-wide cross-link identification. Nat Commun 8, 15473.

- Liu, F., Rijkers, D.T., Post, H., and Heck, A.J. (2015). Proteome-wide profiling of protein assemblies by cross-linking mass spectrometry. Nat Methods 12, 1179-1184.

- Mi, H., Lazareva-Ulitsky, B., Loo, R., Kejariwal, A., Vandergriff, J., Rabkin, S., Guo, N., Muruganujan, A., Doremieux, O., Campbell, M.J., *et al.* (2005). The PANTHER database of protein families, subfamilies, functions and pathways. Nucleic Acids Res 33, D284-288.

- Schatzle, P., Ster, J., Verbich, D., McKinney, R.A., Gerber, U., Sonderegger, P., and Mateos, J.M. (2011). Rapid and reversible formation of spine head filopodia in response to muscarinic receptor activation in CA1 pyramidal cells. J Physiol 589, 4353-4364.

- Schlager, M.A., Kapitein, L.C., Grigoriev, I., Burzynski, G.M., Wulf, P.S., Keijzer, N., de Graaff, E., Fukuda, M., Shepherd, I.T., Akhmanova, A., and Hoogenraad, C.C. (2010). Pericentrosomal targeting of Rab6 secretory vesicles by Bicaudal-D-related protein 1 (BICDR-1) regulates neuritogenesis. EMBO J 29, 1637-1651.

- Spangler, S.A., Schmitz, S.K., Kevenaar, J.T., de Graaff, E., de Wit, H., Demmers, J., Toonen, R.F., and Hoogenraad, C.C. (2013). Liprin-alpha2 promotes the presynaptic recruitment and turnover of RIM1/CASK to facilitate synaptic transmission. J Cell Biol 201, 915-928.

- van Beuningen, S.F.B., Will, L., Harterink, M., Chazeau, A., van Battum, E.Y., Frias, C.P., Franker, M.A.M., Katrukha, E.A., Stucchi, R., Vocking, K., *et al.* (2015). TRIM46 Controls Neuronal Polarity and Axon Specification by Driving the Formation of Parallel Microtubule Arrays. Neuron 88, 1208-1226.

- van der Vaart, B., van Riel, W.E., Doodhi, H., Kevenaar, J.T., Katrukha, E.A., Gumy, L., Bouchet, B.P., Grigoriev, I., Spangler, S.A., Yu, K.L., *et al.* (2013). CFEOM1-associated kinesin KIF21A is a cortical microtubule growth inhibitor. Dev Cell 27, 145-160.

- Vizcaino, J.A., Csordas, A., Del-Toro, N., Dianes, J.A., Griss, J., Lavidas, I., Mayer, G., Perez-Riverol, Y., Reisinger, F., Ternent, T., *et al.* (2016). 2016 update of the PRIDE database and its related tools. Nucleic Acids Res 44, 11033.

- Yuan, B., Latek, R., Hossbach, M., Tuschl, T., and Lewitter, F. (2004). siRNA Selection Server: an automated siRNA oligonucleotide prediction server. Nucleic Acids Res 32, W130-134.